IST1 regulates select endosomal recycling pathways

Amy K. Clippinger[1,3], Teresa V. Naismith[1], Wonjin Yoo[2], Silvia Jansen[1], David J. Kast[1], Phyllis I. Hanson[1,4,*].

[1]Department of Cell Biology and Physiology, Washington University in St. Louis
[2]Department of Biological Chemistry, University of Michigan Medical School
[3]Current address: Department of Biochemistry, University of Washington
[4]Current address: Department of Biological Chemistry, University of Michigan Medical School
*Corresponding author

ABSTRACT

ESCRTs (Endosomal Sorting Complex Required for Transport) are a modular set of protein complexes with membrane remodeling activities that include the formation and release of intralumenal vesicles (ILVs) to generate multivesicular endosomes. While most of the 12 ESCRT-III proteins are known to play roles in ILV formation, IST1 has been associated with a wider range of endosomal remodeling events. Here, we extend previous studies of IST1 function in endosomal trafficking and establish that IST1, along with its binding partner CHMP1B, contributes to scission of early endosomal carriers. Functionally, depleting IST1 impairs delivery of transferrin receptor from early/sorting endosomes to the endocytic recycling compartment and instead increases its rapid recycling to the plasma membrane via peripheral endosomes enriched in the clathrin adaptor AP-1. IST1 is also important for export of mannose 6-phosphate receptor from early/sorting endosomes. Examination of IST1 binding partners on these endosomes revealed that IST1 interacts both with CHMP1B and with the MIT domain-containing sorting nexin SNX15 previously reported to regulate endosomal recycling. Kinetic and spatial analyses showed that SNX15 and IST1 occupy a clathrin-containing subdomain distinct from those previously connected to cargo retrieval or degradation. Using live-cell microscopy we demonstrate that SNX15 and CHMP1B alternately control recruitment of IST1 to this domain on the endosomal perimeter and the base of endosomal tubules. These findings indicate that IST1 plays an important and regulated role in specific recycling pathways from the early/sorting endosome.

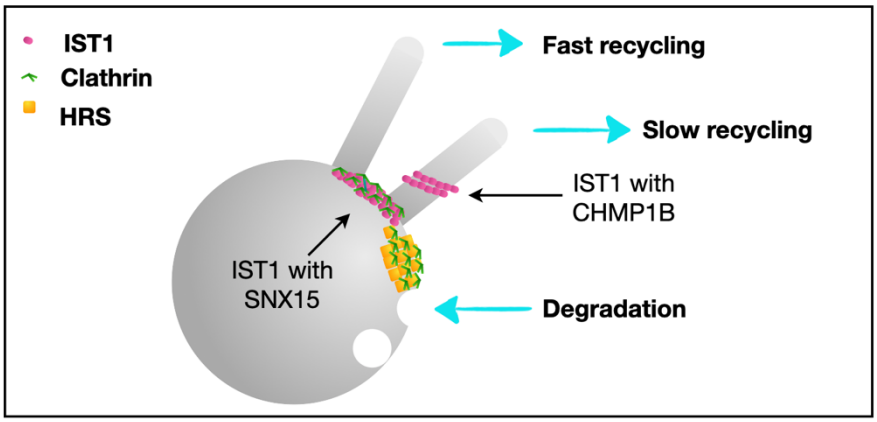

Introduction

ESCRT (Endosomal Sorting Complex Required for Transport)-III proteins are primarily cytosolic monomers that assemble to form membrane-associated filamentous polymers which mediate membrane remodeling events including intraluminal vesicle (ILV) formation, virus budding, nuclear envelope closure, and cytokinetic abscission (Vietri *et al.*, 2020). ESCRT-III proteins contain a “core” ESCRT-III domain that enables homo- and heteropolymer assembly followed by C terminal MIM motifs that interact with MIT domain containing proteins. IST1 is structurally and functionally distinct from other ESCRT-III proteins. Its “core” domain ESCRT-III domain only co-assembles with CHMP1A/1B (Bajorek *et al.*, 2009a) . IST1 also has not one, but two distinct MIM domains, as well as an extended unstructured and proline-rich linker region between its “core” and MIM domains. IST1 interacts via these domains with general ESCRT-III as well as numerous IST1-specific partners (Yang *et al.*, 2008; Renvoisé *et al.*, 2010; Allison *et al.*, 2013, 2017; Maemoto *et al.*, 2014; Chang *et al.*, 2019). Among its best-studied interactors is Vps4 (VPS4A/4B in mammalian cells), the AAA ATPase responsible for disassembling ESCRT-III polymers (Saksena *et al.*, 2009; Adell *et al.*, 2014; Mierzwa *et al.*, 2017). Interestingly, VPS4A mutations that specifically impede release of IST1, but not another ESCRT-III protein CHMP2B, from membranes result in abnormal neurodevelopment (Rodger *et al.*, 2020). Mutations in IST1 specific interactors spastin (SPAST) and spartin (SPART) have also been directly linked to hereditary spastic paraplegia (HSP) (Hazan *et al.*, 1999; Patel *et al.*, 2002; Blackstone *et al.*, 2011).

As might be expected based on its unique structure compared to other ESCRT-III proteins, IST1 has been found to have diverse functional roles in endosomal trafficking across a variety of systems. ESCRT-IIIs, similar to the rest of the ESCRT machinery, are responsible for generating intraluminal vesicles (ILVs) within multivesicular bodies (MVBs) to enable lysosomal degradation and were discovered in a now classic screen for vacuolar protein sorting (vps) mutants (Odorizzi *et al.*, 1998; Babst *et al.*, 2002; Teis *et al.*, 2008). Notably, IST1 was not part of the original set of ESCRT proteins and was instead later identified on the basis of genetic interactions with and structural homology to other ESCRT-III proteins (Rue *et al.*, 2008; Bajorek *et al.*, 2009a, 2009b). IST1 is not required for ILV formation in *Saccharomyces cerevisiae* (Dimaano *et al.*, 2008; Rue *et al.*, 2008; Xiao *et al.*, 2009; Nickerson *et al.*, 2010), plants (Buono *et al.*, 2016), or HeLa cells (Allison *et al.*, 2013). Instead, it has been found to function in endosomal recycling and retrograde trafficking pathways (Allison *et al.*, 2013, 2017, 2019; Laidlaw *et al.*, 2022a). Indeed, its unique assembly with CHMP1B creates constricting filaments around (instead of within) membrane tubules (McCullough *et al.*, 2015) with proposed roles in driving tubule scission (Nguyen *et al.*, 2020; Cada *et al.*, 2022). However, IST1 is also both a negative and positive regulator of Vps4 activity (Tan *et al.*, 2015) and is a positive modulator of MVB biogenesis in yeast (Dimaano *et al.*, 2008; Rue *et al.*, 2008; Xiao *et al.*, 2009; Nickerson *et al.*, 2010). It also controls overall ESCRT recruitment and as a consequence ILV formation during early oocyte maturation in *C. elegans* (Frankel *et al.*, 2017). Altogether, IST1 appears to be a multifunctional ESCRT-III protein.

To gain further insight into the many ways in which IST1 affects endosomal dynamics, we set out to learn more about where and how it functions in endosomal trafficking in cultured human cells. We find that IST1 is enriched on early/sorting endosomes where it localizes with its binding partners SNX15 or CHMP1B to endosomal subdomains that are distinct from those previously known to direct cargo for retrieval/recycling or degradation. Functionally, we find that IST1 is important for slow but not fast transferrin receptor recycling and acts to deliver cargo from early/sorting to recycling endosomes. Our results provide insight into the diversity of machinery controlling pathways out of the early/sorting endosome for dynamic control of cellular membrane organization.

Results

IST1 contributes to scission of tubules on early/sorting endosomes

To broadly assess IST1's contributions to endosomal homeostasis, we asked where and how it functions in two human cell lines, T24 bladder carcinoma and U2OS osteosarcoma cells. An antibody recognizing endogenous IST1 confirmed its localization throughout the cytoplasm, at cell bridges and mid-bodies and on bright punctate structures that based on previous studies are likely to be early/sorting endosomes (Figure 1A) (Agromayor *et al.*, 2009; Allison *et al.*, 2017). Indeed, many of the IST1 marked structures were also immunoreactive for the early endosomal protein EEA1 (Figure 1B, Supplemental Figure S1).

To explore IST1's function, we depleted it using a previously characterized siRNA duplex (Allison *et al.*, 2013, 2017) that reduced IST1 by >90% in both T24 and U2OS cells (Supplemental Figure S2). By immunostaining, we found that cells depleted of IST1 had increased levels of endosomal EEA1 (Figure 1C) consistent with previous reports of IST1 playing a role in maturation of early/sorting endosomes via export of SNX1- and SNX-4 marked tubules (Allison *et al.*, 2013). We confirmed that a second IST1 siRNA duplex similarly decreased IST1 while increasing endosomal EEA1 (Supplemental Figure S2&S3). Previous reports of IST1's participation in endosomal recycling have attributed this to the partnership that we and others described between IST1 and its membrane-proximal binding partner CHMP1B on endosomal tubules (McCullough *et al.*, 2015; Connell *et al.*, 2019; Nguyen *et al.*, 2020b; Cada *et al.*, 2022). To broadly assess the contribution of IST1 and CHMP1B to the dynamics of tubulovesicular carriers emerging from sorting endosomes, we monitored GFP-Rab5b by live-cell spinning disc confocal microscopy (Zeigerer *et al.*, 2012; Rowland *et al.*, 2014). GFP-Rab5b organelles are typically punctate and tubules that occasionally emerge are short-lived (Supplemental Figure S4). After depleting IST1 or CHMP1B, we assessed tubule length and persistence (Figure 1D, Supplemental Figure S5). Depleting either protein increased the frequency and lifetime of these tubules (Figure 1E&F). Although carriers lacking Rab5b (and instead marked by other GTPases, e.g. Rab4a, Rab4b, Rab11) also emerge from these endosomes and were not visualized here, the increase in Rab5b tubules is consistent with a role for both IST1 and CHMP1B in scission of tubulovesicular carriers leaving the sorting endosome.

To assess additional contributions of IST1 to endosomal homeostasis, we immunostained IST1-depleted cells with an antibody that recognizes mono- and poly-ubiquitin conjugated proteins (Fujimuro *et al.*, 1994) to look for abnormalities in processing cargo typically targeted into MVBs for ESCRT-dependent degradation. As expected, depleting CHMP4B increased ubiquitinated material on swollen vacuolar structures (Odorizzi *et al.*, 1998; Yang *et al.*, 2021) (Supplemental Figure S6A arrow). Depleting IST1, however, had no effect on the normal, predominantly nuclear, distribution of ubiquitin conjugates (Supplemental Figure S6B). Together with earlier studies showing that IST1 is not required for efficient EGF receptor degradation (Agromayor *et al.*, 2009) this suggests that IST1 is not generally involved in ESCRT-dependent handling of MVB cargo.

IST1 functions in slow but not fast transferrin recycling

Consistent with previous studies (Allison *et al.*, 2017, 2019), our data point to a primary role for IST1 at the early/sorting endosome. Transferrin (Tfn) and its receptor (TfnR) are responsible for ongoing and essential iron uptake into cells and are widely studied for their robust and readily monitored trafficking through the endosomal system. Multiple pathways recycle internalized TfnR from early/sorting endosomes back to the plasma membrane, classified decades ago as 'fast' and 'slow' based on their kinetics, with distinct molecular players and endosomal compartments responsible for direct *vs*. indirect return of TfnR to the plasma membrane (Maxfield and McGraw, 2004; Grant and Donaldson, 2009). To ask which of these pathways IST1 participates in, we depleted it as above and examined TfnR trafficking. At steady state, immunostaining showed that TfnR was dispersed from its typical juxtanuclear cluster (Figure 2A). We confirmed that this redistribution was caused by IST1 depletion using a second siRNA duplex (Supplemental Figure S7A). To identify the cause and functional impact of this TfnR dispersal, we used imaging based assays (Kalaidzidis *et al.*, 2015; Schindler *et al.*, 2015) to monitor the time-dependent distribution of fluorescently labelled Tfn. Strikingly, IST1-depleted cells accumulated only about half as much Tfn as did controls after a 1 hr loading incubation (Figure 2B). This decrease in the steady-state level of internalized Tfn was not caused by differences in total cellular TfnR (Figure 2C), pointing instead to changes in TfnR trafficking.

The simplest explanation for reduced internal Tfn accumulation would be that the cells internalize less TfnR from the plasma membrane. Indeed, the dispersal of TfnR caused by depleting IST1 indicated a shift in receptor distribution that might have changed the relative amount of TfnR inside vs. outside the cell. Comparison of surface exposed TfnR in control *vs*. IST1-depleted cells showed that antibody-detected TfnR on non-permeabilized cells increased in the absence of IST1 (Figure 2D). However, we also separately monitored the kinetics of uptake of fluorescently labelled Tfn. The total amount of Tfn internalized during a 30 sec pulse of fluorescently tagged Tfn appeared unchanged by depleting IST1 (Figure 2E) although its distribution differed, remaining dispersed in IST1-depleted cells (Figure 2F). Despite IST1 depleted cells having more TfnR on the cell surface (Figure 2D), we found that IST1-depleted cells internalized the same absolute amount of Tfn in a 30 sec pulse (Figure 2E) and also bound the same amount of labeled Tfn when incubated on ice for 30min (Supplemental Figure S7B). This points to changes in recycling rather than a decrease in TfnR endocytosis as the likely explanation for the reduced steady-state level of internal Tfn. Similar changes in peripheral vs juxtanuclear Tfn have previously been associated with an increase in rapid recycling/return to the plasma membrane in cells depleted of proteins involved in slow endosomal recycling including SNX4 (Traer *et al.*, 2007), aftiphilin (Hirst *et al.*, 2005), and Rabenosyn-5 and EHD-1 (Naslavsky *et al.*, 2004). Previous studies showing that IST1-depleted cells contain elongated SNX1- and SNX4-marked tubules (Allison *et al.*, 2013) also support a selective role for IST1 in creating and/or releasing the tubular carriers that mediate transfer from sorting to recycling endosomes.

If rapid recycling is increased, we would expect to see an increase in the rate of Tfn efflux. To monitor efflux, we chased cells loaded to equilibrium with fluorescent Tfn with unlabeled Tfn and quantified remaining fluorescence as a function of time (Figure 2G-I). IST1-depleted cells again accumulated only half as much Tfn as did controls. Although differences in the overall rate of Tfn loss were not apparent, there was high variability in the initial Tfn intensity between cells. Comparing normalized Tfn intensities across individual cells eliminated much variability to reveal an acceleration of early Tfn loss in cells depleted of IST1 (Figure 2I, inset). From our observations we conclude that IST1 is required for a pathway underlying the longer retention of Tfn within the cell (i.e. sorting of TfnR into the slow recycling pathway) but not for its rapid recycling to the cell surface.

A limitation in the sensitivity of our assay arises from using pulses of labeled Tfn because holo-Tfn (iron bound) and apo-Tfn (iron free) have very affinities for TfnR (Yersin *et al.*, 2008), and changes in the trafficking of TfnR within the endosomal system (i.e. trafficking to an acidic endosome where iron is released from Tfn) can affect iron assimilation (Chen *et al.*, 2013) and thus the subsequent exchange of unlabeled for labeled Tfn. This likely is the reason for the discrepancy of IST1 depleted cells having more TfnR on the cell surface but binding and endocytosing the same amount of labeled Tfn as controls. Newly developed methods to rapidly detect TfnR itself, such as using HaloTag (Jonker *et al.*, 2020), will be a way to further study rapid TfnR recycling.

IST1-independent recycling involves AP-1 containing endosomes

Recycling pathways leaving the early/sorting endosome require many factors for both cargo sorting and carrier biogenesis. Prominent among these are retromer, retriever, COMMD/CCDC22/CCDC93 (CCC) complex, the endosomal SNX-BAR sorting complex for promoting exit-1 (ESCPE-1) complex and the associated actin nucleation promoting Wiscott–Aldrich syndrome protein and SCAR homologue (WASH) complex. Clathrin and associated machinery including the adaptor AP-1 also contribute. IST1 is not known to directly bind any of these factors. To better understand the selective effect of depleting IST1 on slow *vs*. fast TfnR recycling we set out to define recycling pathway(s) that remain functional in cells depleted of IST1. Given earlier reports of impaired SNX1- and SNX4-marked carriers (Allison *et al.*, 2013, 2017) and the defect in slow TfnR recycling above, we first focused on clathrin and its adaptor AP-1 that have long been known to participate in rapid recycling (Hirst *et al.*, 2005, 2012; D'Souza *et al.*, 2014; Chamberland *et al.*, 2016). After depleting IST1 we observed a striking redistribution of AP-1 from its typical perinuclear concentration to the cell periphery (Figure 3A). To ask if TfnR accesses these AP-1 marked compartments, we compared the distribution of a Tfn pulse to that of AP-1 γ-adaptin over time (Figure 3A). In the absence of IST1, we again observed that Tfn remained in peripherally localized endosomes following endocytosis. These same endosomes showed a robust AP-1 signal, confirming that peripheral AP-1 compartments are part of the IST1-independent Tfn recycling pathway (Figure 3A). Coincident AP-1 and Tfn was apparent on both punctate and tubular organelles (Figure 3B). This

is consistent with the concept that clathrin coated vesicles bud from tubular endosomal networks (Stoorvogel *et al.*, 1996), and suggests that, in IST1 depleted cells, this is the compartment in which Tfn accumulates for rapid recycling to the PM.

To further characterize this IST1-independent rapid recycling pathway, we took advantage of the selective effects of brefeldin A (BFA) on different elements of the endosomal system. BFA releases Arf1-recruited AP-1 from membranes (Robinson and Kreis, 1992; Wong and Brodsky, 1992), tubulating Rab4a-containing endosomes known for their involvement in rapid recycling with little or no effect on the Rab11 endosomes involved in slow recycling thereby selectively perturbing rapid recycling (Daro *et al.*, 1996). In T24 cells, we found that BFA transiently shifted TfnR from the cell surface into extended tubular compartments (Figure 3C) highlighting the importance of BFA-sensitive pathway(s) for TfnR recycling. Acutely treating IST1-depleted cells with BFA led to even more extensive tubular networks that took longer than their control counterparts to resolve (Figure 3C), consistent with enhanced cargo flux through AP-1 containing endosomes and the rapid recycling pathway.

For further insight into how IST1 affects cargo exit from sorting endosomes, we asked how depleting it affects mannose 6-phosphate receptor (M6PR) trafficking as this receptor has also been reported to move through both retromer and AP-1 marked carriers (Arighi *et al.*, 2004; Saint-Pol *et al.*, 2004; Seaman, 2004; Popoff *et al.*, 2007, 2009). M6PR's primary itinerary includes anterograde export from TGN to endosomes and retrograde transit from various endosomes back to the TGN. At steady state, M6PR is typically concentrated in the perinuclear TGN and/or ERC. Allison et al. have previously reported that loss of IST1 impairs the return of M6PR to the TGN (Allison *et al.*, 2017). In agreement with these findings, we found that cells depleted of IST1 often contained abnormally dispersed M6PR some of which overlapped with EEA1 (Figure 4A&B). Using super-resolution Airyscan confocal imaging, we examined the localization of M6PR and EEA1 in more detail (Figure 4B). We found that while tubules containing M6PR could be seen originating from EEA1 endosomes in both IST1 depleted and control cells, overlap of M6PR and EEA1 around the endosomal perimeter was increased in IST1 depleted cells compared to control cells (Figure 4B). This suggests that IST1 is needed for efficient sorting of M6PR from early/sorting endosomes into tubules for exit from endosome. Altogether, the observed changes in TfnR and M6PR trafficking point to an important role for IST1 on the early/sorting endosome in events needed to create and/or release carriers that mediate delivery to the ERC and/or TGN. The compensatory increase in rapid recycling highlights the plasticity of trafficking events on sorting endosomes.

IST1 and SNX15 occupy a distinct subdomain on sorting endosomes

Given the role of IST1 in a subset of pathways leaving sorting endosomes we next wanted to know when it is present on these organelles. To kinetically define early/sorting endosomes, we incubated cells with fluorescently tagged Tfn for 2-3 minutes. Immunostaining for EEA1 and IST1 revealed that Tfn rapidly reached compartments containing both of these proteins (Figure 5A). Notably, IST1 was present in discrete spots adjacent to but not overlapping with EEA1 on the endosomal perimeter, suggesting that it localizes to a subdomain distinct from where EEA1 resides. Once endosomes acquire EEA1, confocal fluorescence microscopy can usually resolve "degradative" and "retrieval" subdomains marked respectively by HRS (ESCRT-0) or retromer and associated sorting nexins together with branched actin (Cullen and Steinberg, 2018). To ask whether IST1 puncta coincide with markers of either of these subdomains we compared its localization with that of the retromer protein VPS35 and the ESCRT-0 component HRS. We also examined sorting nexin 15 (SNX15) previously implicated in regulating recycling (Feng *et al.*, 2016) and shown to arrive on newly formed endosomes with similar timing to HRS (Danson *et al.*, 2013; Flores-Rodriguez *et al.*, 2015). Inspection of immunostained cells revealed that IST1 did not colocalize well with either HRS or VPS35 but appeared to overlap with SNX15 (Figure 5B). However, the juxtanuclear concentration of endosomes made it difficult to study the relationships among these factors in any detail.

To enable spatial and temporal resolution of endogenous proteins as they are recruited to nascent endosomes, we depolymerized microtubules to block their centripetal movement and perinuclear clustering. We then monitored different proteins on individual endosomes marked by newly internalized cargo (Derivery *et al.*, 2009, 2012). For an endocytic marker, we used fluorescently labelled wheat germ agglutinin (WGA), a lectin

which binds to and is internalized with sialic acid and N-acetylglucosamine (GlcNAc) moieties on the plasma membrane (Chazotte, 2011) (Raub *et al.*, 1990). We internalized pre-bound WGA for 5 min as outlined schematically in Figure 6A before immunostaining (Figure 6B). We then examined the relationship among different signals on endosomes (or regions of interest (ROIs)) marked by internalized WGA (Figure 6C&D).Most, but not all, WGA containing endosomes were marked by EEA1 (Figure 6C empty arrow head, Supplemental Figure S9A), and approximately 60% of EEA1-marked endosomes acquired WGA during the 5 minute pulse (Figure 6C filled arrow heads, Supplemental Figure S9A).

Using this experimental set-up we interrogated the relationship between IST1 and markers of different endosomal subdomains. A commonly used approach for assessing correlation in light microscopy is to determine if there is a linear relationship between the intensity of two signals within each pixel (i.e. Spearman's rank coefficient or Pearson's correlation coefficient). This analysis will, however, miss signals that are juxtaposed but not directly overlapping with each other. These can be detected using ROI-based analysis to detect correlation of two signals present on the same endosome. By comparing pixel- and ROI-based analyses we can assess and distinguish co-localization vs. co-occurrence of relevant proteins on these endosomes.

Using this approach, we observed that IST1 exhibited poor pixel-based correlation with EEA1 or HRS (Figure 6D, x axis). In contrast, IST1 had a higher pixel-based correlation with SNX15. This suggests that IST1 colocalizes with SNX15 but not with EEA1 or HRS. When we then assessed the ROI-based correlation of IST1 with EEA1 and HRS (Figure 6D, y axis), the signals were more correlated (both using the Spearman's rank coefficient shown here and Pearson's correlation analysis in Supplemental Figure S9B). This quantification indicates that although IST1 did not colocalize with EEA1 and HRS it may be present on the same endosomes.

With this analytical approach we next wanted to explore the relationship between SNX15/IST1 and factors associated with the retrieval/recycling subdomain (Cullen and Steinberg, 2018). We examined VPS35 relative to HRS, SNX15 and EEA1. VPS35 showed poor pixel-based correlation (Figure 6E, x axis) and increased ROI-based correlation (Figure 6E, y axis) with all three signals. This confirmed previous reports of the proximal but non-overlapping relationship between HRS and VPS35 (Norris *et al.*, 2017; MacDonald *et al.*, 2018). Additionally our observations of a proximal but non-overlapping relationship between VPS35 and SNX15 is similar to the report that IST1 is adjacent to SNX1 (Allison *et al.*, 2017), given the colocalization we observed between IST1 and SNX15 and the known colocalization of VPS35 and SNX1. Taken together, these studies define what appear to be three separable protein domains on early/sorting endosomes – one marked by HRS, one by VPS35, and one by SNX15. This adds a new subdomain containing SNX15 and IST1 to the early endosomal surface, extending earlier characterizations of retrieval/recycling and degradative domains (Norris *et al.*, 2017; Cullen and Steinberg, 2018).

IST1 co-assembles with sorting nexin 15 on endosomes

Given the presence of IST1 and SNX15 in a common subdomain on the early/sorting endosome, we next asked whether there is a direct interaction between these two proteins. IST1, like other ESCRT-III proteins, has C-terminal "MIM" motifs that bind to MIT domains to mediate specific protein-protein interaction. SNX15 is a MIT domain-containing protein recruited to endosomes via a PX domain that binds phosphatidyl-inositol-3-phosphate (Phillips *et al.*, 2001; Danson *et al.*, 2013) (Figure 7B). Its MIT domain shares ~30% homology with MIT domains in VPS4A/VPS4B but had until recently (Wenzel *et al.*, 2022) not been shown to bind ESCRT-III proteins. To explore a possible interaction between SNX15 and IST1 in cells, we co-overexpressed them in U2OS cells. In agreement with previous observations using yeast two-hybrid interaction analyses (Danson *et al.*, 2013), we found that the ESCRT-III proteins CHMP1 – CHMP7 did not co-assemble with SNX15 (data not shown). IST1-mApple, however, strikingly colocalized with SNX15-GFP on discrete structures spread across the cell (Figure 7A, inset Figure 7A). The presence of internalized Tfn within these structures, as well as within protruding tubules, confirmed their identity as endosomes (Figure 7A).

If SNX15 helps bring IST1 to the membrane, we predicted that its overexpression would recruit endogenous IST1 to the endosome. Indeed, overexpressing SNX15 led to a striking redistribution of IST1 onto endosomes with a corresponding depletion from the cytoplasm (Supplemental Figure S10A). To determine how IST1 engages with SNX15, we asked if removing its N-terminal "core" ESCRT-III domain affected assembly with

SNX15 (Figure 7B). We found that the C-terminal fragment (CTD) of IST1 was still recruited to the endosome by over-expressed SNX15, albeit to a lesser extent than full length IST1 (Figure 7C). To further define the sequences responsible for interaction between these proteins, we deleted the C-terminal MIM1 motif from the IST1 CTD fragment and found that this abolished its SNX15-mediated recruitment to endosomes (Figure 7C). Conversely, we removed the MIT domain from SNX15 and found that this fragment no longer depleted IST1mApple from the cytoplasm (Supplemental Figure S10B). Together with a biochemical characterization of binding between SNX15's MIT domain and IST1 reported by Wenzel et al. while we were preparing this manuscript (Wenzel *et al.*, 2022), these changes indicate that an IST1 MIM1-SNX15 MIT domain interaction provides a novel mechanism by which IST1 can be recruited to early/sorting endosomes independently of other ESCRT proteins.

SNX15 and CHMP1B alternately distribute IST1 between endosomal subdomains

Having found that IST1 and SNX15 co-assemble to form a specific subdomain on the endosome, we wanted to define their relationship with other endosome-associated proteins (Figure 8A-D). We used cells stably expressing low levels of SNX15gfp for this analysis. Similar to what we had observed for the relationship of VPS35 with SNX15, we found that other retrieval domain components such as the WASH complex (FAM21 and WASH), retromer associated sorting nexin SNX1, and branched actin-associated cortactin showed minimal colocalization with SNX15gfp as assessed by Pearson's correlation coefficient, however, all were present within an adjacent subdomain on the majority of SNX15gfp positive endosomes (Figure 8E, insets in Figure 8A-D).

Given that both SNX15 and CHMP1B directly bind to endosomal membranes, we wondered if they cooperate to engage IST1. This seemed possible because of their distinct binding to IST1, with CHMP1B engaging the core ESCRT-III domain in IST1 and SNX15 its C-terminal MIM motifs (see above). Interestingly, we found that despite their known interaction, there was no CHMP1B within the IST1-SNX15 enriched subdomain (Figure 8A). This suggested that IST1 might assemble with CHMP1B exclusively at sites devoid of SNX15, potentially where tubules emerge from endosomes. To determine if this is the case, we compared CHMP1B's localization to markers of branched actin known to be present at the base of endosomal tubules (Cullen and Steinberg, 2018). Indeed, we saw examples of CHMP1B coincident with cortactin (Figure 8C). Using live cell imaging to better characterize the relationship between SNX15 and actin, we confirmed that SNX15gfp was nearly always restricted to the vacuolar endosome, with an intensity that decreases near and around puncta marked by actin (Figure 8F). We could however see a transient "finger" of SNX15gfp signal extend along the same direction as the actin domain, but still showed very little direct overlap with actin (Figure 8F, arrow and asterisk). These live imaging results demonstrate that IST1 assembled with SNX15 is restricted to the vacuolar domain of endosomes, and our colocalization results indicate that IST1 is not able to interact or assemble with its binding partner CHMP1B when assembled with SNX15.

Clathrin is well known for its role in endocytosis at the PM, but also functions intracellularly at the trans-Golgi network and on endosomes. It participates in endosomal recycling and localizes to nascent vesicles along endosomal tubules. Additionally, clathrin forms a "flat" clathrin domain on early/sorting where it plays an essential role in regulating the dynamics of HRS and the kinetics of ILV formation. Our results above indicate that IST1 is not required for either of these clathrin-based processes. However, SNX15 has also been reported to bind clathrin (Danson *et al.*, 2013) and we wondered if SNX15 and IST1 together might associate with clathrin. Although the overall correlation of SNX15gfp and clathrin signals was relatively low (Figure 8E), there is clear overlap between these two signals (Figure 8D). We also observed non-overlapping clathrin signal that was nonetheless associated with tubular structures originating from SNX15GFP endosomes (Figure 8D and 8E, left panel). To explore potential roles for SNX15GFP in regulating endosomal clathrin, we examined live cells transiently expressing mRFP clathrin light chain A (CLCa) and SNX15GFP and confirmed overlap of SNX15GFP with mRFP CLCa (Figure 9A arrow) with a higher Pearson's correlation coefficient than with endogenous proteins (Supplemental Figure S11A&B), granted the level of clathrin intensity was lower than on other places on the endosome (Figure 9A arrowheads). We also again detected "fingers" of SNX15GFP, and these colocalized with the bright mRFP CLCa tubular and punctate structures originating from the endosome (Figure 9A arrow heads) and confirmed that Tfn was present in clathrin-marked tubules that protrude from SNX15GFP endosomes (Supplemental Figure S11C).

Clathrin that localizes with HRS to the degradative domain has been shown to be devoid of clathrin adaptors such as AP-1. To ask if the clathrin signal that colocalizes with SNX15 on the vacuolar domain or on tubular structures, largely devoid of SNX15, corresponds to nascent clathrin coated vesicles, we stained cells expressing SNX15GFP for the clathrin adaptor AP-1. We could see collections of AP-1 signal originating from SNX15 endosomes but not overlapping with SNX15 (Figure 9B). We also did not observe SNX15 co-localizing with any other clathrin adaptor (GGA2, GGA1, EpsinR) (data not shown), indicating that the clathrin associated with SNX15 and IST1 on the vacuolar domain is likely non-functional in regard to forming clathrin-coated buds. However, by light microscopy we cannot resolve whether this is a clathrin coated domain or contiguous clathrin coated buds that lack the adaptors we imaged, and future EM studies will be required to establish the nature of clathrin assembled with SNX15 and IST1.

Given how the function of IST1 seems to be independent of clathrin's known functions on the endosome, we next queried the relationship between IST1 and clathrin when it was assembled with SNX15 or CHMP1B. We compared the localization of IST1GFP with mRFP CLCa when it was assembled with either SNX15 or CHMP1B (Figure 9C-E). While IST1 mainly co-localized with clathrin on the vacuolar domain when assembled with SNX15, it could also be detected in dim "finger" structures that coincided with bright CLCa signal, similar to what we had seen for SNX15 (Figure 9D). In contrast, IST1/CHMP1B co-polymers transiently co-localized with CLCa signal that was not associated with the vacuolar domain (Figure 9E). Moreover, both complexes of IST1GFP colocalized with CLCa, but the colocalization was much stronger when assembled with SNX15 (Figure 9C). Our live cell-imaging of IST1GFP in different complexes, strongly suggests that IST1 has multiple functions which could include a role in the dynamics of sorting in a "flat" clathrin domain when assembled with SNX15 and a role in the fission of recycling tubules when assembled with CHMP1B. While IST1 colocalizes with clathrin to different degrees when assembled with SNX15 and CHMP1B, our functional data suggests that the clathrin-regulated processes of ILV formation and rapid recycling occur in the absence of IST1, indicating that IST1 is important for diverting cargo from these two pathways into the slow recycling pathway (Figure 9F).

Discussion

Functional studies in both yeast and mammalian cells have previously uncovered roles for IST1 in endosomal recycling (Allison *et al*., 2013; Allison *et al*., 2017, Laidlaw *et al*., 2022). The ability of IST1 to polymerize around and constrict tubules coated with CHMP1B (McCullough *et al*., 2015) suggested it could do so by promoting scission of endosomal tubules, but where and when this happens and how IST1 cooperates with other machinery involved in endosomal sorting and scission has been unclear. Our analysis of Rab5 tubule dynamics confirms a role for IST1 and CHMP1B in scission, similar to that previously shown for the WASH complex (Derivery *et al*., 2009) and potentially controlled by contact with the endoplasmic reticulum (Rowland *et al*., 2014) or microtubules (Cada *et al*., 2022). However, there are many trafficking pathways out of Rab5 endosomes mediated by diverse factors and it was not clear what specific recycling pathways IST1 might regulate. By studying TfnR trafficking with its broad and readily studied itinerary, we found that depleting IST1 impairs delivery of TfnR from the early/sorting endosome into the "slow" or indirect recycling pathway. This was accompanied by increased flux through the "fast" pathway directly to the plasma membrane. Notably, IST1-independent "fast" recycling moved through organelles marked by the clathrin adaptor AP-1, which together with clathrin is known for its involvement in fast recycling (Hirst *et al.*, 2005, 2012; D'Souza *et al.*, 2014; Chamberland *et al.*, 2016). Interestingly, AP-1 itself may be involved in aspects of fast as well as slow recycling of Tfn. Depleting either the γ subunit of AP-1 (Hirst *et al.*, 2005) or the AP-1 accessory protein NECAP-2 (Chamberland *et al.*, 2016) impairs rapid recycling of TfnR supporting an essential role for AP-1 in this process. In contrast, and similar to IST1, depleting two other AP-1 accessory proteins aftiphilin and p200/HEAT repeat-containing protein 5b (HTR5B) impair delivery of Tfn to the ERC and increase fast recycling through peripheral compartments (Hirst *et al.*, 2005).

We also found that M6PR, a cargo that recycles between sorting endosomes and the ERC and/or TGN, was mislocalized in IST1 depleted cells. This is again consistent with a role for IST1 in transporting cargo from the sorting endosome to the ERC. Previous work has shown that IST1 mediates resolution of SNX1 tubules (Allison *et al.*, 2013, 2017) that may be representative of a broader set of tubular trafficking intermediates. Interestingly Laidlaw *et al*. recently found that Ist1p and Vps4p localize to both the PVC (where retromer and

sorting nexins have been shown to reside), as well as to non-PVC structures (Laidlaw *et al*., 2022). This suggests that IST1 could be involved in multiple events with distinct players. In our cells, we found that IST1 and SNX15 localize to the same endosomes as VPS35 but in a different subdomain. Further work will be needed to better understand the relationship between IST1 and different "slow" recycling machinery.

Interestingly, we also found that SNX15 (and SNX15/IST1) did not overlap with HRS. However, they did overlap significantly with clathrin. This suggests that there could be multiple distinct "flat" clathrin domains present on endosomes may not be exclusively populated by HRS as suggested previously (Cullen and Steinberg, 2018). It might also suggest that the clathrin within the SNX15 subdomain might have a different role than clathrin in the HRS subdomain. The ability of HRS to bind clathrin is important for cargo sorting into ILVs (Wenzel *et al.*, 2018), so could clathrin bound to SNX15 be important for cargo recycling? We also found that clathrin not only associated with SNX15/IST localized on the vacuole, but also to tubular structures protruding from SNX15 positive endosomes. While IST1 mainly co-localized with clathrin on the vacuolar domain when assembled with SNX15, it could also be seen, albeit weakly, along the base of clathrin positive tubules. We found that AP-1 did not localize to the SNX15 domain, but could be seen in clusters by SNX15 endosomes, likely on the clathrin-positive tubules observed by live cell. Ultrastructure of recycling tubules containing clathrin coated buds as well as TfnR were visualized decades ago (Stoorvogel *et al.*), and more recently populations of dynamic or "gyrating" peripheral clathrin and GGA1 (presumed to be clathrin buds on waving tubules) that are also positive for Tfn have been imaged in live cells but are not well understood (Zhao and Keen, 2008; Derivery *et al.*, 2012; Luo *et al.*, 2013; Majeed *et al.*, 2014) Rab4 marked endosomes have Tfn positive tubules that are also decorated with AP-1 and GGA adaptors (D'Souza *et al.*, 2014). Overexpression of SNX15 seems to enables the clear visualization of both the clathrin-coated tubule and the originating endosome, but it is not clear if there is a functional relationship between the SNX15/IST1 "flat" clathrin domain and AP-1/clathrin coated tubule. On the other hand, these results agree with the localization and function of yeast Ist1 to an early endosome that is distinct from the PVC populated by retromer and its associated sorting nexins.

Finally, we found that the interaction between IST1 and SNX15 was direct and required the MIM1 domain of IST1. We also observed that while the "core" ESCRT domain of IST1 was not required for IST1 to interact with SNX15, it was required for all cytoplasmic IST1 to be dramatically redistributed to SNX15 coated endosomes. This could indicate that the interaction between SNX15 and IST1 is synergistic, likely via avidity based-interactions. This raises the question of what confirmation IST1 adopts when assembled with SNX15. If IST1 behaved like other ESCRT-IIIs it would be expected to polymerize in an open confirmation. Alternatively, IST1 could maintain its ability to polymerize in the closed state, even though it is not assembled with CHMP1B. Does the assembly of IST1 with CHMP1B cause IST1 to switch from an open polymer state with SNX15 to a close polymer state? A greater understanding of what confirmation IST1 adopts when assembled with SNX15 compared to CHMP1B is warranted, as it is clear that SNX15 and CHMP1B drive the localization of IST1 to very distinct locations on the endosomes.

Acknowledgements: Some imaging experiments were performed in part through the use of Washington University Center for Cellular Imaging (WUCCI) supported by Washington University School of Medicine, The Children's Discovery Institute of Washington University and St. Louis Children's Hospital (CDI-CORE-2015-505 and CDI-CORE-2019-813) and the Foundation for Barnes-Jewish Hospital (3770 and 4642). In particular, confocal/super-resolution data was generated on a Zeiss LSM 880 Airyscan Confocal Microscope which was purchased with support from the Office of Research Infrastructure Programs (ORIP), a part of the NIH Office of the Director under grant OD021629. This research was supported by NIH grants R01GM076686 (P.I.H.), R01GM136925 (D.J.K), R01GM138448 (S.J.) and R01NS050717 (P.I.H.); and NSF fellowship DGE-1143954 (A.K.C.).

Materials and Methods

Materials:

All chemical reagents were purchased from Sigma-Aldrich unless otherwise indicated. Compounds were used at the following concentrations unless explicitly stated: 10 μM Nocodozole, 10 μM Brefeldin A. Concentrated stock solutions of all compounds were prepared in dimethyl sulfoxide (Nocodozole) or methanol (Brefeldin A) and stored at -80°C in single-use aliquots. Conjugates of Transferrin to Alexa Fluor 5565 (Cat # T35352 Invitrogen) and unlabeled Holo-Transferrin (Sigma) were used at the stated concentrations. GFP-Rab5A was a gift from Phillip Stahl (Washington University in St. Louis) and has been described in (Chen *et al.*, 2014). LifeAct-mTagBFP2 was a gift from David Kast (Washington University in St. Louis) and has been described (Riedl *et al.*, 2008). mEmerald-Clathrin-15 was a gift from Michael Davidson (Addgene plasmid # 54040 ; http://n2t.net/addgene:54040 ; RRID:Addgene_54040) (Fiolka *et al.*, 2012). mRFP-Clc was a gift from Ari Helenius (Addgene plasmid # 14435 ; http://n2t.net/addgene:14435 ; RRID:Addgene_14435) (Tagawa *et al.*, 2005). Cortactin-pmCherryC1 was a gift from Christien Merrifield (Addgene plasmid # 27676 ; http://n2t.net/addgene:27676 ; RRID:Addgene_27676) (Taylor *et al.*, 2011). Apple-N1 was a gift from Michael Davidson (Addgene plasmid # 54567 ; http://n2t.net/addgene:54567 ; RRID:Addgene_54567) (Shaner *et al.*, 2008). IST1 isoform A (NM_001270975.1, NP_001257904.1) and SNX15 full length or truncations as indicated were subcloned into pEGFP-N1, pcDNA4TO and mApple-N1. CHMP1B cDNA (NM_020412.4) and IST1 isoform A was recloned into pcDNA4 to create untagged CHMP1B and IST1.

Antibodies:

The following antibodies were used for immunofluorescence at the listed concentration:

Antibody	Species	Company	Catalog #	Concentration
CHMP1B	Rabbit (polyclonal)	Proteintech	14639-1-AP	1:200
EEA1	Mouse (monoclonal)	BD Transduction Laboratories	610456	1:1000
IST1	Rabbit (polyclonal)	Proteintech	19842-1-AP	1:000
c-myc	Mouse (monoclonal)	Developmental Studies Hybridoma Bank	9E+10	1:500
FK2	Mouse (monoclonal)	Biomol/Enzo	PW8810	1:1000

p230	Mouse (monoclonal)	BD Transduction Laboratories	G88620	1:400
SNX15	Mouse (monoclonal)	Santa Cruz	sc-393430	1:200
HRS	Mouse (monoclonal)	Enzo	ALX-804-382	1:1000
VPS35	Rabbit (polyclonal)	Thermo Scientific		1:500
clathrin heavy chain (X22)	Mouse (monoclonal)	GeneTex	GTX22731	1:1000
Cortactin (4F11)	Mouse (monoclonal)	Millipore	05-180	1:250
WASH	Rabbit (polyclonal)	Kind gift from Billadeau Lab MC2058	N/A	1:500
AP-1	Mouse (monoclonal)	Kind gift from Kornfeld Lab clone 100/3	N/A	1:500
M6PR	Rabbit (polyclonal)	Kind gift from Kornfeld Lab	N/A	1:1000
CHMP4B	Rabbit (polyclonal)	Kind gift from Shiels Lab	N/A	1:200
TfnR	Mouse (monoclonal)	Santa Cruz	sc-32272 (3B8 2A1)	1:500

Goat anti-rabbit and mouse secondary antibodies conjugated to Alexa 488, 555 or 647 were from Molecular Probes (Thermo Fisher).

Cell culture:

U2OS, T24, and COS-7 cells originally derived from ATCC were cultured in DMEM or McCoy's (for T24 cells) (Invitrogen) with 8-10% FBS (Atlanta Biologicals). All cells were maintained at 37°C and supplemented with 5% CO2. GFPRab5B, IST1GFP, SNX15GFP stable lines were generated by placing transfected cells under selection for neomycin resistance with 500µg/mL Geneticin (Invitrogen).

Plasmid Transfections:

Cells were transfected with the indicated plasmid(s) using Lipofectamine 2000 following the manufacturer's instructions and used for experiments within 16–24 hr. For immunostaining and live cell imaging, U2OS cells were reverse transfected (i.e. plated and transfected at the same time). Cells were plated onto glass slips

(#1.5, Electron Microscopy Sciences) or 35 mm glass bottom dishes with #1.5 cover glass (Cellvis) and imaged or fixed 12-18hrs later.

siRNA treatment

All siRNA duplexes used have been previously validated or used as indicated below. The following sequences were synthesized by Dharmacon and used at the following concentrations:

IST1 #1 (50nM) 5′-GCAAAUACGCCUUUCUCAUdTdT-3′ (Allison *et al.*, 2013)

IST1 #2 (40 nM) 5'GGCCUUAUCCAGUCAUAUGAdTdT-3'

CHMP1B (25nM) 5'-UGGACAAAUUCGAGCACCAdTdT-3' (Morita *et al.*, 2011)

Control (non-targeting firefly luciferase) (25nM) 5′-AUGUAUUGGCCUGUAUUAG-dTdT-3') (Skowyra *et al.*, 2018)

Control LAP1 (25nM) 5'-CGUCUUUCCUCUAGUACUA-3' (Goodchild *et al.*, 2015)

Control (Silencer Select Negative Control #1 siRNA (Ambion, cat no 4390843)

CHMP4B (25nM) 5'-CGAUAAAGUUGAUGAGUUAdTdT-3' (Morita *et al.*, 2011)

Cells were plated at 90,000 (T24) or 150,000 (U2OS) per 6 well dish, and 3-5 hrs after plating cells were transacted using DharmaFECT 1 (Dharmacon) according to manufacturer's instructions. Cells were replated after 24 hrs on to slips or live cell dishes, either uncoated or coated with fibronectin (10µg/mL Fibronectin for 1hr at RT, washed 2X in PBS, then covered in media before cells added), as indicated. The cells were then imaged or fixed after 48 hrs of siRNA treatment. Alternatively, after 24 hrs IST1 siRNA treated cells were replated and transfected with a second IST1 siRNA transfection. These cells were replated onto slips after 24 hrs, and then fixed after a total of 96 hrs of siRNA treatment. When ESCRT-III siRNA treated cells were mixed with control siRNA cells before plating on slips (as indicated), immunofluorescence was used to identify ESCRT-III depleted cells.

Immunoblotting:

Proteins from whole cell lysates were separated by SDS–PAGE and transferred to nitrocellulose. Blots were incubated with primary antibodies against IST1 or TfnR followed by HRP conjugated secondary antibodies in

Tris-buffered saline containing 0.1% Tween-20 and 5% milk. Proteins were detected by chemiluminescence using a ChemiDoc MP imaging system (BioRad).

Microscopy:

The following light microscope platforms were used for imaging.

Microscope Platform	**1 Widefield fluorescence**	**2 Spinning disk confocal**	**3 Spinning disk confocal**	**4 Spinning disk confocal**	**5 Airy Scan confocal**
Microscope	Olympus IX-81	Olympus IX-81 (same as Platform 1)	Nikon Ti-E inverted	Nikon Eclipse Ei2 inverted	Zeiss LSM 880
Objective(s)	60X, 1.42 NA oil immersion (PLAPON)	60X, 1.42 NA oil immersion (PLAPON Apochromat)	60X1.4 NA oil immersion (CFI Plan Apochromat Lambda)	60X1.4 NA and 100X 1.45 NA oil immersion (CFI Plan Apochromat Lambda)	63X, 1.40 oil immersion Plan Apochromat
Light Source/Lasers	Ex-Cite 120Q (Excelitas)	Two-line (488 and 561nm) Sapphire laser module (Coherent)	Four-line (405, 488, 561, 647nm)	Four-line (405, 488, 561, 647nm)	Six-line (405, 488, 561, 647nm used)
Spinning disk	N/A	CSU10 (Yokogawa)	CSU-X1 (Yokagawa)	CSU-W1 (Yokogawa)	N/A
Camera	ORCA-Flash 2.8 scientific CMOS (Hamamatsu Photonics)	Cascade B12 (Photometrics)	Zyla 4.2-megapixel scientific CMOS camera (Andor)	ORCA-Flash 4.0 scientific CMOS (Hamamatsu Photonics)	Airy Scan Detector
Acquisition software	Metamorph Advanced software	mManager	Nikon Elements	Nikon Elements	Zeiss ZEN
Live cell imaging chamber	N/A	Tokai Hit INU series stage-top incubator	N/A	Tokai Hit STX stable top incubator	N/A

Tfn live cell exocytosis assay:

Cells were plated on p35 dishes with 1.5 coverslip glass bottoms (MatTek) one day before imaging. 10ug/mL Alexafluor Tfn555 was added in normal cell media (8% serum in McCoys media for T24 or DMEM for U2OS). Prior to Tfn incubation, dishes were transferred to live cell imaging chamber on microscope (Platform 4). Several positions to image (221x221 μm^2 regions) were selected across the dish. After 1hr Tfn555 media was removed. Cells were washed with 1mL of PBS followed by 2mL of chase media consisting of full media with

200ug/mL unlabeled Tfn. A z-stack (0.25um step size) was acquired for each pre-selected cell region every 2.5 minutes for 30 minutes (for T24 cells) or every 5 minutes for 1 hr (for U2OS cells).

Tfn live cell exocytosis assay analysis. Images of individual cells were cropped into individual files. The 0min Tfn image was used to draw a mask containing a single cell. Each slice of the time series was background subtracted using a ROI from a dish region adjacent to the cell. A maximum intensity Z projection was created for each time series. A second ROI based subtraction followed by a constant background subtraction was taken to reduce signal outside of cells to zero. The Tfn intensity was then measured for each timepoint and reported as mean Tfn intensity across each cell. To normalize Tfn signals, the total Tfn intensity (integrated density) within each cell at each time point was divided by the total Tfn intensity within the cell at the 0min time point.

Tfn Pulse Assay:

We monitored the kinetics with which a labeled pulse of Tfn moves into and through the cell as optimized (Kalaidzidis *et al.*, 2015). T24 cells were fed 20ug/uL Alexafluor 555 transferrin (Molecular Probes) for 30 seconds (cells on slip inverted on drop of pulse media). This incubation was done at 37°C (dry-hot bath) in serum-free pulse media containing either 1:1 HBSS and McCoy's Media or McCoy's Media buffered with by 25mM HEPES to maintain pH. After pulse, slips were dropped into ice-cold serum free media to wash excess Tfn and then transferred to 37°C serum free media to continue endocytosis for 1.5min (2min total). Slips were then transferred to Chase media, consisting of serum containing media with 200ug/mL unlabeled Tfn, and allowed to incubate at 37°C (in incubator) for the indicated time. Alternatively, we also used a shorter pulse by washing slips in ice cold serum free media for 1.5 minutes after the 30 second pulse, before place in chase media for indicated times. This limited the uptake to the pulse time alone. For assessing total Tfn binding, cells were incubated with labeled Tfn (inverted on a drop of pulse media) on ice for 30 min and washed in ice cold PBS before freezing. All slips were frozen in < -20°C methanol followed by fixation and immunostaining as below.

Immunofluorescence Microscopy:

Cells were fixed using using two approaches: either cross-linking fixative alone (paraformaldehyde) followed by TX-100, or precipitation fixation (-20°C methanol) followed by rehydration in cross-linking fixative (bis(sulfosuccinimidyl)suberate) as described in (Bhattacharyya *et al.*, 2010). For cross-linking fixative, cells were incubated in 3% PFA, 4% sucrose for 20 minutes, and then permeabilized with either 0.1% saponin or 0.1% Triton for 10 min (as indicated). For quantification of TfnR present on cell surface, cells were fixed in 3% PFA, 4% sucrose and then immediately processed for staining without permeabilization. Methanol + BS3 fixed cells were process as described (Bhattacharyya *et al.*, 2010) with the slight modification that 12mm slips were dropped in 5mL of methanol in a 15mL conical tube, precooled to -80C to ensure that the methanol was <-20°C when slips were added. All subsequent IF steps were identical for both processes, starting with inverting the slips on blocking buffer (1hr at RT), and then in primary antibodies in block (overnight at 4°C), washing, as described in (Bhattacharyya *et al.*, 2010), and then inverting in secondary antibodies in block (30min at RT), washing, and mounting in gelvatol. Fixed cells were imaged on platforms 1-5 as indicated.

Image Analysis and Quantification of immunostained cells:

ROIs were traced to define masks containing individual cells. For quantification of signal within masked area, image stacks were subjected to 50pixel rolling background subtraction (unless otherwise noted) in FIJI prior to preparing a maximum intensity projection. Max projections were further background subtracted to set cytoplasmic and/or dark noise to zero, and all images within the same experiment were treated identically. Image processing and analysis was completed with custom-written scripts in FIJI. Alternatively, max projections and masks were imported into Matlab using Bio-Formats (Linkert *et al.*, 2010). Custom-written scripts, using the Matlab Image Processing Toolbox, were used for image analysis to measure intensities, channel correlations, and dispersal using K-means clustering. K-means clustering analysis was performed on the highest intensity pixels within a given cell—with the number of pixels depending on the area to be counted and the resolution of the image. The distances of each pixel from the identified K-means center for the cell was then plotted in a histogram. Equivalent binning was used for replicate cells so that the pixel count per bin could be averaged for all cells of a particular condition. Image processing scripts are available upon request. Quantification of SNX15GFP endosomes positive for endosomal markers (Figure 8E) was done using

threshold-defined ROIs of SNX15GFP with the scorer assessing if each ROI contained or was immediately adjacent to other endosomal markers.

Brefeldin A Assay:

IST1 siRNA treated cells and control cells were either plated together onto glass slips the day before BFA treatment. Cells were fixed before or after incubation in 10uM BFA in normal media at the indicated times. T24 cells were stained with IST1 (to distinguish control and IST1 depleted cells) and TfnR. Tubular networks induced by BFA were assessed by a blinded scorer counting the number of continuous tubular structures longer than 12μm.

Rab5 tubule quantification:

Movies of GFP-Rab5b cells were acquired on Platform 2. 33ms exposures were collected every 2s over 30 sec. To quantify tubule length and duration, we segmented Rab5bgfp labelled endosomes in each image using a model-based segmentation algorithm (Paul *et al.*, 2013) implemented in the Fiji plugin Squassh (Rizk *et al.*, 2014). As described (Rizk *et al.*, 2014), the segmentation mask assigns each pixel a value (0-1) based on its probability of belonging to an object and is the result of simultaneous image denoising, deconvolution, and segmentation. Using Squassh, background was subtracted from the original image with a rolling ball window of 10 pixels. Segmentation was determined using a theoretical PSF model calculated for our spinning disk microscope, a regularization parameter of 0.05, and a Poisson noise model. Using MATLAB (MathWorks), the resulting segmentation mask was converted into a binary image by thresholding to include only the top 3% of pixel values (representing the 3% of pixels most likely to belong to an object). ROIs were determined from connected thresholded regions, and only ROIs with an eccentricity of greater than 0.7 and a major axis length of greater than 20 pixels (5μm) were considered, empirically chosen to eliminate the majority of ROIs corresponding to non-tubular or short tubular endosomes. Note that this length criterion provides a conservative estimate of tubule length as tubules that are not linear (i.e. bent or curved) and are actually longer than 5μm are excluded. A blind scorer then determined if the remaining ROIs, or 'tubule candidates', were actual tubules (to be scored) or a cluster of endosomes (not to be scored) for every frame analyzed. See fig. S5 for further details and example of quantification.

WGA Assay:

U2OS cells were washed in ice cold PBS and inverted on drop containing 2.5ug/mL TRITC labeled WGA (2.5mg/mL) in serum-free pulse media containing 1:1 HBSS and McCoy's Media. WGA-TRITC was allowed to bind for 30 minutes, then slips were washed in ice-cold serum free media for 1 minute. Slips were either fixed in PFA or allowed to endocytose WGA-TRITC labeled proteins at 37°C. Slips were transferred to serum free DMEM with or without 10uM nocodozole at 37°C (in incubator) for different intervals (5-15 minutes). Slips were either fixed in PFA (retaining PM associated WGA) or were washed in ice-cold PBS with 0.1M GlcNAc (Sigma) for 2 minutes and then fixed in PFA (to compete off WGA-TRITC bound to PM). Cells were then permeabilized (as described) and stained with antibodies.

WGA Assay analysis. Cells were imaged using Platform 3. A z-stack was acquired for each image. Background subtraction (with rolling ball radius of 3 pixels or 270nm) was performed in image J for each slice. A maximum intensity projection of the stack was then used for analysis, Background intensity levels of non-cell area was confirmed to be zero, and additional background (150) was subtracted across all pixels and all channels to remove diffuse signal within the cell. WGA and EEA1 ROIs were then defined by using an additional threshold of 150, so as to exclude smaller, less bright WGA or EEA1 signal. Once these ROIs were defined they were dilated by two pixels (180nm) so as to include any signal immediately adjacent to them. The ROI-based correlation was the Pearson's or Spearman's coefficient between the sum intensity of two signals within the ROI, while the pixel-based correlation was the Pearson's or Spearman's coefficient between the intensity of the two signals within the pixels contained in the ROI. Nocodozole treatment was critical to disperse endocytosed material to allow assignment of signal within a specified region to a particular endosome. To determine if WGA or EEA1 ROIs were positive for a signal, the following procedure was used: if a WGA or EEA1 ROI contained any non-zero signal (from the background subtracted image) it was counted at EEA1, WGA, HRS, or SNX15 positive.

Statistical Analysis

Data was graphed and statistical analysis was performed in Prism. Statistical tests were used as described.

Transmission Electron Microscopy

T24 cells were plated onto fibronectin coated sapphire disks. Cells were high pressure frozen using a Leica EM High-Pressure Freezer (WUCCI core). Prior to immediate freezing cells were kept at 37C in 1:1 McCoy's and HBSS to maintain pH. Samples were freeze substituted using Leica EM AF2S Freeze Substitution System (WUCCI core) and subsequently sectioned and imaged using the TEM described above.

References

Adell, MAY, Vogel, GF, Pakdel, M, Müller, M, Lindner, H, Hess, MW, and Teis, D (2014). Coordinated binding of Vps4 to ESCRT-III drives membrane neck constriction during MVB vesicle formation. J Cell Biol 205, 33–49.

Agromayor, M, Carlton, JG, Phelan, JP, Matthews, DR, Carlin, LM, Ameer-Beg, S, Bowers, K, and Martin-Serrano, J (2009). Essential Role of hIST1 in Cytokinesis. Mol Biol Cell 20, 1374–1387.

Allison, R et al. (2017). Defects in ER-endosome contacts impact lysosome function in hereditary spastic paraplegia. J Cell Biol 216, 1337–1355.

Allison, R, Edgar, JR, and Reid, E (2019). Spastin MIT Domain Disease-Associated Mutations Disrupt Lysosomal Function. Front Neurosci 13, 1179.

Allison, R, Lumb, JH, Fassier, C, Connell, JW, Martin, D Ten, Seaman, MNJ, Hazan, J, and Reid, E (2013). An ESCRT-spastin interaction promotes fission of recycling tubules from the endosome. J Cell Biol 202, 527–543.

Arighi, CN, Hartnell, LM, Aguilar, RC, Haft, CR, and Bonifacino, JS (2004). Role of the mammalian retromer in sorting of the cation-independent mannose 6-phosphate receptor. J Cell Biol 165, 123–133.

Babst, M, Katzmann, DJ, Estepa-Sabal, EJ, Meerloo, T, and Emr, SD (2002). Escrt-III: an endosome-associated heterooligomeric protein complex required for mvb sorting. Dev Cell 3, 271–282.

Bajorek, M, Morita, E, Skalicky, JJ, Morham, SG, Babst, M, and Sundquist, WI (2009a). Biochemical Analyses of Human IST1 and Its Function in Cytokinesis. Mol Biol Cell 20, 1360–1373.

Bajorek, M, Schubert, HL, McCullough, J, Langelier, C, Eckert, DM, Stubblefield, WMB, Uter, NT, Myszka, DG, Hill, CP, and Sundquist, WI (2009b). Structural basis for ESCRT-III protein autoinhibition. Nat Struct Mol Biol 16, 754–762.

Bhattacharyya, D, Hammond, AT, and Glick, BS (2010). High-quality immunofluorescence of cultured cells. Methods Mol Biol 619, 403–410.

Blackstone, C, O'Kane, CJ, and Reid, E (2011). Hereditary spastic paraplegias: membrane traffic and the motor pathway. Nat Rev Neurosci 12, 31–42.

Buono, RA, Paez-Valencia, J, Miller, ND, Goodman, K, Spitzer, C, Spalding, EP, and Otegui, MS (2016). Role of SKD1 Regulators LIP5 and IST1-LIKE1 in Endosomal Sorting and Plant Development. Plant Physiol 171, 251–264.

Cada, AK et al. (2022). Friction-driven membrane scission by the human ESCRT-III proteins CHMP1B and IST1. Proc Natl Acad Sci U S A 119, e2204536119.

Chamberland, JP, Antonow, LT, Santos, MD, and Ritter, B (2016). NECAP2 controls clathrin coat recruitment to early endosomes for fast endocytic recycling.

Chang, C-L et al. (2019). Spastin tethers lipid droplets to peroxisomes and directs fatty acid trafficking through ESCRT-III. J Cell Biol 218, 2583–2599.

Chazotte, B (2011). Labeling membrane glycoproteins or glycolipids with fluorescent wheat germ agglutinin. Cold Spring Harb Protoc 2011, pdb.prot5623.

Chen, C et al. (2013). Snx3 Regulates Recycling of the Transferrin Receptor and Iron Assimilation. Cell Metab 17, 343–352.

Chen, P-I, Schauer, K, Kong, C, Harding, AR, Goud, B, and Stahl, PD (2014). Rab5 Isoforms Orchestrate a "Division of Labor" in the Endocytic Network; Rab5C Modulates Rac-Mediated Cell Motility. PLoS One 9, e90384.

Connell, JW, Allison, RJ, Rodger, CE, Pearson, G, Zlamalova, E, and Reid, E (2019). ESCRT-III-associated proteins and spastin inhibit protrudin-dependent polarised membrane traffic. Cell Mol Life Sci, 1–18.

Cullen, PJ, and Steinberg, F (2018). To degrade or not to degrade: mechanisms and significance of endocytic recycling. Nat Rev Mol Cell Biol 19, 679–696.

D'Souza, RS, Semus, R, Billings, EA, Meyer, CB, Conger, K, and Casanova, JE (2014). Rab4 orchestrates a small GTPase cascade for recruitment of adaptor proteins to early endosomes. Curr Biol 24, 1187–1198.

Danson, C et al. (2013). SNX15 links clathrin endocytosis to the PtdIns3P early endosome independently of the APPL1 endosome. J Cell Sci 126, 4885–4899.

Daro, E, van der Sluijs, P, Galli, T, and Mellman, I (1996). Rab4 and cellubrevin define different early endosome populations on the pathway of transferrin receptor recycling. Proc Natl Acad Sci U S A 93, 9559–9564.

Derivery, E, Helfer, E, Henriot, V, and Gautreau, A (2012). Actin Polymerization Controls the Organization of WASH Domains at the Surface of Endosomes. PLoS One 7, e39774.

Derivery, E, Sousa, C, Gautier, JJ, Lombard, B, Loew, D, and Gautreau, A (2009). The Arp2/3 Activator WASH Controls the Fission of Endosomes through a Large Multiprotein Complex. Dev Cell 17, 712–723.

Dimaano, C, Jones, CB, Hanono, A, Curtiss, M, and Babst, M (2008). Ist1 Regulates Vps4 Localization and Assembly. Mol Biol Cell 19, 465–474.

Feng, T, Niu, M, Ji, C, Gao, Y, Wen, J, Bu, G, Xu, H, and Zhang, Y-W (2016). SNX15 Regulates Cell Surface Recycling of APP and Aβ Generation. Mol Neurobiol 53, 3690–3701.

Fiolka, R, Shao, L, Rego, EH, Davidson, MW, and Gustafsson, MGL (2012). Time-lapse two-color 3D imaging of live cells with doubled resolution using structured illumination. Proc Natl Acad Sci U S A 109, 5311–5315.

Flores-Rodriguez, N, Kenwright, DA, Chung, P-H, Harrison, AW, Stefani, F, Waigh, TA, Allan, VJ, and Woodman, PG (2015). ESCRT-0 marks an APPL1-independent transit route for EGFR between the cell surface and the EEA1-positive early endosome. J Cell Sci 128, 755–767.

Frankel, EB, Shankar, R, Moresco, JJ, Yates, JR, Volkmann, N, and Audhya, A (2017). Ist1 regulates ESCRT-III assembly and function during multivesicular endosome biogenesis in Caenorhabditis elegans embryos. Nat Commun 8, 1439.

Fujimuro, M, Sawada, H, and Yokosawa, H (1994). Production and characterization of monoclonal antibodies specific to multi-ubiquitin chains of polyubiquitinated proteins. FEBS Lett 349, 173–180.

Goodchild, RE, Buchwalter, AL, Naismith, T V, Holbrook, K, Billion, K, Dauer, WT, Liang, C-C, Dear, ML, and Hanson, PI (2015). Access of torsinA to the inner nuclear membrane is activity dependent and regulated in the endoplasmic reticulum. J Cell Sci 128, 2854–2865.

Grant, BD, and Donaldson, JG (2009). Pathways and mechanisms of endocytic recycling. Nat Rev Mol Cell Biol 10, 597–608.

Hazan, J et al. (1999). Spastin, a new AAA protein, is altered in the most frequent form of autosomal dominant spastic paraplegia. Nat Genet 23, 296–303.

Hirst, J, Borner, GHH, Antrobus, R, Peden, AA, Hodson, NA, Sahlender, DA, and Robinson, MS (2012). Distinct and overlapping roles for AP-1 and GGAs revealed by the “knocksideways” system. Curr Biol 22, 1711–1716.

Hirst, J, Borner, GHH, Harbour, M, and Robinson, MS (2005). The Aftiphilin/p200/-Synergin Complex. Mol Biol Cell 16, 2554–2565.

Jonker, CTH, Deo, C, Zager, PJ, Tkachuk, AN, Weinstein, AM, Rodriguez-Boulan, E, Lavis, LD, and Schreiner, R (2020). Accurate measurement of fast endocytic recycling kinetics in real time. J Cell Sci 133.

Kalaidzidis, I, Miaczynska, M, Brewińska-Olchowik, M, Hupalowska, A, Ferguson, C, Parton, RG, Kalaidzidis, Y, and Zerial, M (2015). APPL endosomes are not obligatory endocytic intermediates but act as stable cargo-sorting compartments. J Cell Biol 211, 123–144.

Laidlaw, KME, Calder, G, and MacDonald, C (2022a). Recycling of cell surface membrane proteins from yeast endosomes is regulated by ubiquitinated Ist1. J Cell Biol 221.

Laidlaw, KME, Calder, G, and MacDonald, C (2022b). Recycling of cell surface membrane proteins from yeast endosomes is regulated by ubiquitinated Ist1. J Cell Biol 221.

Linkert, M et al. (2010). Metadata matters: access to image data in the real world. J Cell Biol 189, 777–782.

Luo, Y, Zhan, Y, and Keen, JH (2013). Arf6 Regulation of Gyrating-Clathrin. Traffic 14, 97–106.

MacDonald, E et al. (2018). HRS-WASH axis governs actin-mediated endosomal recycling and cell invasion. J Cell Biol 217, 2549–2564.

Maemoto, Y, Ono, Y, Kiso, S, Shibata, H, Takahara, T, Sorimachi, H, and Maki, M (2014). Involvement of calpain-7 in epidermal growth factor receptor degradation via the endosomal sorting pathway. FEBS J 281, 3642–3655.

Majeed, SR et al. (2014). Clathrin light chains are required for the gyrating-clathrin recycling pathway and thereby promote cell migration. Nat Commun 5, 3891.

Maxfield, FR, and McGraw, TE (2004). Endocytic recycling. Nat Rev Mol Cell Biol 5, 121–132.

McCullough, J et al. (2015). Structure and membrane remodeling activity of ESCRT-III helical polymers. Science 350, 1548–1551.

Mierzwa, BE et al. (2017). Dynamic subunit turnover in ESCRT-III assemblies is regulated by Vps4 to mediate membrane remodelling during cytokinesis. Nat Cell Biol 19, 787–798.

Morita, E, Sandrin, V, McCullough, J, Katsuyama, A, Baci Hamilton, I, and Sundquist, WI (2011). ESCRT-III protein requirements for HIV-1 budding. Cell Host Microbe 9, 235–242.

Naslavsky, N, Boehm, M, Backlund, PS, and Caplan, S (2004). Rabenosyn-5 and EHD1 Interact and Sequentially Regulate Protein Recycling to the Plasma Membrane. Mol Biol Cell 15, 2410–2422.

Nguyen, HC, Talledge, N, McCullough, J, Sharma, A, Moss, FR, Iwasa, JH, Vershinin, MD, Sundquist, WI, and Frost, A (2020). Membrane constriction and thinning by sequential ESCRT-III polymerization. Nat Struct Mol Biol 27, 392–399.

Nickerson, DP, West, M, Henry, R, and Odorizzi, G (2010). Regulators of Vps4 ATPase Activity at Endosomes Differentially Influence the Size and Rate of Formation of Intralumenal Vesicles. Mol Biol Cell 21, 1023–1032.

Norris, A, Tammineni, P, Wang, S, Gerdes, J, Murr, A, Kwan, KY, Cai, Q, and Grant, BD (2017). SNX-1 and RME-8 oppose the assembly of HGRS-1/ ESCRT-0 degradative microdomains on endosomes. Proc Natl Acad Sci U S A 114, E307–E316.

Odorizzi, G, Babst, M, and Emr, SD (1998). Fab1p PtdIns(3)P 5-kinase function essential for protein sorting in the multivesicular body. Cell 95, 847–858.

Patel, H, Cross, H, Proukakis, C, Hershberger, R, Bork, P, Ciccarelli, FD, Patton, MA, McKusick, VA, and Crosby, AH (2002). SPG20 is mutated in Troyer syndrome, an hereditary spastic paraplegia. Nat Genet 31, 347–348.

Paul, G, Cardinale, J, and Sbalzarini, IF (2013). Coupling Image Restoration and Segmentation: A Generalized Linear Model/Bregman Perspective. Int J Comput Vis 104, 69–93.

Pfitzner, A-K, Mercier, V, Jiang, X, Moser von Filseck, J, Baum, B, Šarić, A, and Roux, A (2020). An ESCRT-III Polymerization Sequence Drives Membrane Deformation and Fission. Cell 182, 1140-1155.e18.

Phillips, SA, Barr, VA, Haft, DH, Taylor, SI, and Haft, CR (2001). Identification and characterization of SNX15, a novel sorting nexin involved in protein trafficking. J Biol Chem 276, 5074–5084.

Popoff, V et al. (2009). Analysis of articulation between clathrin and retromer in retrograde sorting on early endosomes. Traffic 10, 1868–1880.

Popoff, V, Mardones, GA, Tenza, D, Rojas, R, Lamaze, C, Bonifacino, JS, Raposo, G, and Johannes, L (2007). The retromer complex and clathrin define an early endosomal retrograde exit site. J Cell Sci 120, 2022–2031.

Raub, TJ, Koroly, MJ, and Roberts, RM (1990). Rapid endocytosis and recycling of wheat germ agglutinin binding sites on CHO cells: evidence for two compartments in a nondegradative pathway. J Cell Physiol 144, 52–61.

Renvoisé, B, Parker, RL, Yang, D, Bakowska, JC, Hurley, JH, and Blackstone, C (2010). SPG20 protein spartin is recruited to midbodies by ESCRT-III protein Ist1 and participates in cytokinesis. Mol Biol Cell 21, 3293–3303.

Riedl, J et al. (2008). Lifeact: a versatile marker to visualize F-actin. Nat Methods 5, 605–607.

Rizk, A, Paul, G, Incardona, P, Bugarski, M, Mansouri, M, Niemann, A, Ziegler, U, Berger, P, and Sbalzarini, IF (2014). Segmentation and quantification of subcellular structures in fluorescence microscopy images using Squassh. Nat Protoc 9, 586–596.

Robinson, MS, and Kreis, TE (1992). Recruitment of coat proteins onto Golgi membranes in intact and permeabilized cells: Effects of brefeldin A and G protein activators. Cell 69, 129–138.

Rodger, C et al. (2020). De Novo VPS4A Mutations Cause Multisystem Disease with Abnormal Neurodevelopment. Am J Hum Genet 107, 1129–1148.

Rowland, AA, Chitwood, PJ, Phillips, MJ, and Voeltz, GK (2014). ER Contact Sites Define the Position and Timing of Endosome Fission. Cell 159, 1027–1041.

Rue, SM, Mattei, S, Saksena, S, and Emr, SD (2008). Novel Ist1-Did2 Complex Functions at a Late Step in Multivesicular Body Sorting. Mol Biol Cell 19, 475–484.

Saint-Pol, A et al. (2004). Clathrin adaptor epsinR is required for retrograde sorting on early endosomal membranes. Dev Cell 6, 525–538.

Saksena, S, Wahlman, J, Teis, D, Johnson, AE, and Emr, SD (2009). Functional reconstitution of ESCRT-III assembly and disassembly. Cell 136, 97–109.

Schindler, C, Chen, Y, Pu, J, Guo, X, and Bonifacino, JS (2015). EARP is a multisubunit tethering complex involved in endocytic recycling. Nat Cell Biol 17, 639–650.

Seaman, MNJ (2004). Cargo-selective endosomal sorting for retrieval to the Golgi requires retromer. J Cell Biol 165, 111–122.

Shaner, NC, Lin, MZ, McKeown, MR, Steinbach, PA, Hazelwood, KL, Davidson, MW, and Tsien, RY (2008). Improving the photostability of bright monomeric orange and red fluorescent proteins. Nat Methods 5, 545–

551.

Skowyra, ML, Schlesinger, PH, Naismith, T V, and Hanson, PI (2018). Triggered recruitment of ESCRT machinery promotes endolysosomal repair. Science 360, eaar5078.

Stoorvogel, W, Oorschot, V, and Geuze, HJ A Novel Class of Clathrin-coated Vesicles Budding from Endosomes.

Stoorvogel, W, Oorschot, V, and Geuze, HJ (1996). A novel class of clathrin-coated vesicles budding from endosomes. J Cell Biol 132, 21–33.

Tagawa, A, Mezzacasa, A, Hayer, A, Longatti, A, Pelkmans, L, and Helenius, A (2005). Assembly and trafficking of caveolar domains in the cell: caveolae as stable, cargo-triggered, vesicular transporters. J Cell Biol 170, 769–779.

Tan, J, Davies, BA, Payne, JA, Benson, LM, and Katzmann, DJ (2015). Conformational Changes in the Endosomal Sorting Complex Required for the Transport III Subunit Ist1 Lead to Distinct Modes of ATPase Vps4 Regulation. J Biol Chem 290, 30053–30065.

Taylor, MJ, Perrais, D, and Merrifield, CJ (2011). A high precision survey of the molecular dynamics of mammalian clathrin-mediated endocytosis. PLoS Biol 9, e1000604.

Teis, D, Saksena, S, and Emr, SD (2008). Ordered assembly of the ESCRT-III complex on endosomes is required to sequester cargo during MVB formation. Dev Cell 15, 578–589.

Traer, CJ, Rutherford, AC, Palmer, KJ, Wassmer, T, Oakley, J, Attar, N, Carlton, JG, Kremerskothen, J, Stephens, DJ, and Cullen, PJ (2007). SNX4 coordinates endosomal sorting of TfnR with dynein-mediated transport into the endocytic recycling compartment. Nat Cell Biol 9, 1370–1380.

Vietri, M, Radulovic, M, and Stenmark, H (2020). The many functions of ESCRTs. Nat Rev Mol Cell Biol 21, 25–42.

Wenzel, DM, Mackay, DR, Skalicky, JJ, Paine, EL, Miller, MS, Ullman, KS, and Sundquist, WI (2022). Comprehensive analysis of the human ESCRT-III-MIT domain interactome reveals new cofactors for cytokinetic abscission. Elife 11.

Wenzel, EM, Schultz, SW, Schink, KO, Pedersen, NM, Nähse, V, Carlson, A, Brech, A, Stenmark, H, and Raiborg, C (2018). Concerted ESCRT and clathrin recruitment waves define the timing and morphology of intraluminal vesicle formation. Nat Commun 9, 2932.

Wong, D, and Brodsky, F (1992). 100-kD proteins of Golgi- and trans-Golgi network-associated coated vesicles have related but distinct membrane binding properties. J Cell Biol 117, 1171–1179.

Xiao, J, Chen, X-W, Davies, BA, Saltiel, AR, Katzmann, DJ, and Xu, Z (2009). Structural Basis of Ist1 Function and Ist1–Did2 Interaction in the Multivesicular Body Pathway and Cytokinesis. Mol Biol Cell 20, 3514–3524.

Yang, D, Rismanchi, N, Benoıˆt Renvoisé, B, Lippincott-Schwartz, J, Blackstone, C, and Hurley, JH (2008). Structural basis for midbody targeting of spastin by the ESCRT-III protein CHMP1B.

Yang, X, Reist, L, Chomchai, DA, Chen, L, Arines, FM, and Li, M (2021). ESCRT, not intralumenal fragments, sorts ubiquitinated vacuole membrane proteins for degradation. J Cell Biol 220.

Yersin, A, Osada, T, and Ikai, A (2008). Exploring transferrin-receptor interactions at the single-molecule level. Biophys J 94, 230–240.

Zeigerer, A et al. (2012). Rab5 is necessary for the biogenesis of the endolysosomal system in vivo. Nature 485, 465–470.

Zhao, Y, and Keen, JH (2008). Gyrating Clathrin: Highly Dynamic Clathrin Structures Involved in Rapid Receptor Recycling. Traffic 9, 2253–2264.

Figure Legends

Figure 1. ***IST1 functions on early/sorting endosomes in tubule scission (A)*** *U2OS cell stained for endogenous IST1, asterisk denote IST1 at cytokinetic cell bridges and mid-bodies.* ***(B)*** *U2OS (right) and T24 (left) cells immunostained with IST1 and EEA1.* ***(C)*** *Immunostaining of EEA1 in control and IST1 siRNA treated T24 cells, and the recruitment of EEA1 is quantitated to the right, n= 17 for control, n=19 for IST1siRNA treated. Graph shows median ± 95% CI. Statistical analysis with Mann Whitney U test showed significant increase in EEA1 in IST1 depleted cells. These results were observed for 3 independent experiments. Images in (A-C) are max intensity projections.* ***(D-F)*** *Stable U2OS cell lines expressing GFP-Rab5 were treated with IST1, CHMP1B, or the unrelated protein LAP1 (control) siRNA and Rab5 tubule number and duration were assessed by live cell imaging.* ***(D)*** *Representative single frames, single slices from live cell movies. Note the presence of long tubules (inset) in cells depleted of CHMP1B and IST1.* ***(E)*** *Each dot in the scatter plots shows the number of tubules in a single cell longer than 5 µm and present for >2 sec over a 30 sec recording, n=50 for all three groups (results are pooled from three independent experiments). Graph shows median ± 95% CI. Statistical analysis using Kruskal-Wallis test revealed increased number of tubules per cell for IST1 and CHMP1B depleted cells.* ***(F)*** *Bar graph totals tubules counted in (E) and further shows how long each was present (tubule duration). Not only did CHMP1B and IST1 KD cells have more tubules, but only 5 tubules observed in control KD cells persisted for over 4 seconds while 43 and 14 tubules observed in CHMP1B and IST1 KD cells, respectively, persisted for over 4 seconds. Scale bars in the whole cells and insets are as follows: (A) 25 µm, (B) 25 µm and 1 µm, (C) 25 µm, and (D) 25µm and 5 µm, respectively.*

Figure 2. ***Tfn retention within the cell is impaired in IST1 depleted cells. (A****) T24 cells individually treated with control or IST1 siRNA and then mixed and plated together and stained for TfnR (shown) and IST1 (not shown)****.*** ***(B)*** *T24 cells treated with control or IST1 siRNA were incubated with Tfn Alexa 555 for 1 hr, washed with PBS, and imaged immediately after adding chase media containing excess unlabeled Tfn. Quantification of mean intensity of Tfn at time 0 min. Graph shows mean± 95% CI. Control siRNA and IST1 siRNA treated cells n=110,120 (n number pooled from 3 independent experiments with n=26,25 n=42,44 n=42,51), respectively. Statistical analysis using student's t test showed significant decrease in Tfn levels in IST1 depleted cells.* ***(C)*** *Immunoblots of TfnR and IST1 from lysates of cells depleted of IST1 or LAP1 (control) siRNA* ***(D)*** *Quantification of non-permeabilized cells immunolabeled with antibody against the extracellular domain of TfnR to assess TfnR levels on PM. Each point (n =4 for Control and IST1 siRNA treated cells) represents average TfnR intensity area for a field of cells (containing > 5 cells) normalized by the number of nuclei (i.e. average TfnR intensity per cell). Graph shows median ± 95% CI. Statistical analysis using Mann Whitney test showed significant increase in TfnR levels on PM in IST1 depleted cells. This significant increase was replicated in two more independent experiments.* ***(E)*** *Diagram of pulse Tfn assay and quantification of T24 cells allowed to internalize a 30 second pulse of Tfn 555, washed for 1.5 minutes and then chased with unlabeled Tfn. Cells were fixed at the points indicated, n=15, 12, 12, 18, 15, 21, 17 (control) and n=14, 13, 11, 17, 18, 12 ,12 (IST1 KD). Graph shows median ± 95% CI. Statistical analysis using 2-way ANOVA showed Tfn uptake was not impaired in IST1 depleted cells****.*** ***(F)*** *Fluorescence of Tfn in IST1 siRNA treated and control T24 cells that were fixed (at the indicated times) after internalizing a 30 second pulse of Tfn 555. To compare the localization of Tfn signals, the distribution of an equivalent area (4 µm^2) of the highest intensities was assessed by K-means clustering (see Supplemental Figure S8). The distances of each pixel from the determined cell center was plotted in a histogram. The histograms shown are an average of n=18, 21, and 17 for control and n=17,12, and 12 for IST1siRNA treated cells at 2, 3, and 4min, respectively. Similar results were observed for 3 independent experiments. All cell images are max intensity projections.* ***(G)*** *Diagram of the Tfn load-chase assay.* ***(H&I)*** *Time-dependent decay of mean Tfn intensity, measured at 2.5 min intervals after the start of the chase****.*** *(H) shows selected time points of 0,5, and 10 minutes* and *(I) is quantification of all timepoints, n=26 for control siRNA and n=25 IST1 siRNA cells****.*** *Error bars are SEM. Inset in I is internal Tfn Intensity normalized for each cell for 0, 2.5, and 5 min timepoints. Control siRNA and IST1 siRNA treated cells n=110,120 (3 independent experiments with n=26,25 n=42,44 n=42,51), respectively.* ***Graph shows mean*** *± 95% CI. Statistical analysis using 2 way ANOVA showed Tfn exocytosis was faster at 2.5 minutes in IST1 depleted cells. Scale bars in whole cells in (A), (B), (F) and (H) are 25 µm.*

Figure 3. ***Dispersed Tfn positive compartments in IST1 depleted cells are associated with the endosomal clathrin adaptor AP-1*** *(****A)*** *Control (upper panel) or IST1 depleted T24 cells (lower panel) were*

treated with 30 second pulse of Tfn555, washed and allowed to continue endocytosis of bound Tfn for 1.5 minutes before being chased with unlabeled Tfn. Cells were fixed at 30 seconds (1st panel), 1.5 minutes (2nd panel), 2.5 minutes (3rd panel) or 4 minutes (4th panel) and stained for AP-1. ***(B)*** *Diagram of a short Tfn pulse, where a 30 sec pulse of labeled Tfn is immediately followed by chase media, and examples of Control KD and IST1 KD cells where IST1 KD cells show AP-1 localization along abnormal peripheral Tfn tubules. The Spearman's Correlation Coefficient between AP-1 and Tfn was quantified for three independent experiments, total of n= 65 and n= 76 for control and IST1 siRNA treated cells. Graph shows median and 95% ± CI, and statistical analysis using Mann-Whitney test showed significant increase in overlap of AP-1 and Tfn in IST1 depleted cells* ***(C)*** *Mixed IST1 siRNA and control T24 cells were fixed before and after treatment with 10 μM brefeldin A (BFA) for 0, 10, 15 minutes and stained for TfnR (shown) and IST1 (not shown). All cell images are max intensity projections. Tubules longer than 12 μm within tubular networks were quantified at 0,5,10,15,30,60 minutes. n ≥ 10 for each condition, Statistical analysis using 2-way ANOVA demonstrated increased tubulation in IST1 depleted cells at 10 and 15 min. Scale bars in whole cells in (A), (B) and (C) are 25 μm, scale bar in insets in (B) is 2.5 μm.*

Figure 4. ***IST1 depletion causes M6PR to accumulate in EEA1-labeled early/sorting endosomes.*** *(A) To compare the localization of M6PR signals, the distribution of an equivalent area (4 μm^2) of the highest intensities was assessed by K-means clustering (as shown previously for Tfn in Supplemental Figure S8). The distances of each pixel from the determined cell center was plotted in a histogram. The histograms shown are an average of n=25 for control and IST1siRNA treated cells (data shown is compiled from 3 independent experiments with each demonstrating increased dispersed M6PR in IST1 siRNA treated cells).* ***(B)*** *Immunostaining of M6PR and EEA1 in control and IST1 depleted cells. Images are maximum projections of z-stacks obtained on Zeiss LSM 880 with Airyscan and subsequent Airyscan processing. Contrast adjustments on M6PR channel are equivalent for both conditions, but are different for the EEA1 channel, due to increased EEA1 recruitment in IST1 depleted cells. Scale bars in the whole cells and insets are as follows: (B) 10 μm and 1 μm, respectively.*

Figure 5. ***IST1 is proximal to early endosome markers HRS, VPS35, and SNX15.*** *IST1 is proximal to recently endocytosed Tfn and known early/sorting endosome domain markers* ***(A)*** *T24 cells allowed to internalize a 30 second pulse of Tfn 555 and were fixed after 2.5 min and stained for IST1 and EEA1.* ***(B)*** *T24 cells stained for IST1 and either HRS, VPS5 or SNX15. All cell images are max intensity projections. Whole cells and insets are as follows: (A) 25 μm and 1 μm, (B) 25 μm and 1 μm, respectively.*

Figure 6. ***Endogenous IST1 co-localizes with SNX15 on early/sorting endosomes.*** *(**A**) Schematic of the WGA assay. (1) U2OS cells are incubated on ice with WGA-TRITC for 30 min and either fixed in PFA* ***(B, left****), or (2) allowed to internalize bound WGA for 5 min at 37 °C in the presence of nocodazole* ***(B, right),*** *and then stained for EEA1. Images in B are single slices. (**C**) Cells treated identically as B, but (3) washed in ice cold GlcNAc prior to fixation to remove remaining plasma membrane associated WGA, and then stained for two makers. The first set of panels shows WGA signal, which was used to generate WGA ROIs (green outlines) shown with EEA1 and IST1 at the bottom. The remaining two sets of panels show either IST1 or VPS35 co-stained with either HRS or SNX15. Cell images are max intensity projections. (**D**) A plot of the Spearman's rank coefficient of pixel-based vs ROI-based correlations of IST1 relative to EEA1 (n=10), HRS (n=12) or SNX15 (n=10).* ***(E)*** *A plot of the Spearman's rank coefficient of pixel-based vs ROI-based correlations of VPS35 relative to EEA1 (n=10), HRS (n=10) or SNX15 (n=10). Scale bars in the whole cells and/or insets are as follows: (B) 25 μm and 5 μm, respectively; (C) 25 μm, 5 μm, and 1 μm respectively.*

Figure 7. ***IST1 uniquely associates with SNX15.*** ***(A)*** *IST1 and SNX15 co-assemble on Tfn-containing endosomes in living U2OS cells. Cell images are single slices.* ***(B)*** *Domain diagram of IST1 (top), SNX15 (bottom), and constructs used to examine the interaction between IST1 and SNX15.* ***(C)*** *Fixed cells expressing SNX15myc with GFP-tagged IST1 constructs shown in B, in the inverted magenta-green images overlapping signal is black and captures dynamic range of IST1 constructs recruited to SNX15. Cell images are max intensity projections. Scale bars in the whole cells and insets are as follows: (A) 25 μm and 5 μm, respectively; (C) 25 μm and 1 μm, respectively.*

Figure 8*. IST1 assembled with CHMP1B localizes to tubules associated with endosomes, which is distinct from the localization of SNX15. (A-D)** *SNX15gfp stable cells were fixed either with methanol +BS3 (A, C and D) or with PFA (B), and stained with the indicated antibodies of FAM21/SNX1, WASH/cortactin, CHMP1B/cortactin, or IST1/clathrin. All images were deconvolved using Nikon software. Cell images (A-D) are max intensity projections.* ***(E) *Quantification of the pearson's correlation coefficient of SNX15GFP and the indicated marker (left) and manual quantification of the presence of the indicated marker (except for IST1) proximal to SNX15gfp endosomes defined as ROIs (right).* ***(F)*** *Live cell imaging, deconvolved using Nikon software. U2OS cell expressing exogenous SNX15gfp, BFP LifeAct, and mcherry cortactin. Panel to the left shows time-lapse imaging of inset SNX15GFP endosome, as well as line scans that bisect the endosome and the actin domain. Images are single slices. Scale bars in whole cells and insets are as follows: (A-D) 25 µm and 1 µm (F) 5µm and 1 µm, respectively.*

Figure 9.* IST1 assembled with SNX15 but not CHMP1B strongly associates with vacuolar clathrin.** ***(A) *U2OS cells expressing SNX15GFP and mRFP CLCa. Inset panels show separate and merged channels of ROI.The relationship of SNX15 and clathrin on the vacuolar domain is denoted by arrow and on the tubular domain by arrow heads. Images are single slices.* ***(B)*** *U2OS cell expressing SNX15gfp and stained for AP-1, image is max intensity projection. The inset demonstrates collections of AP-1 puncta originating from SNX15gfp positive endosomes (empty arrow heads).* ***(C-E)*** *U2OS cells expressing IST1GFP/SNX15myc or IST1GFP/CHMP1B with mRFP CLCa. Images are single slices. The extent of colocalization between GFP tagged IST1 constructs and mRFP CLCa when assembled with SNX15myc or CHMP1B is quantified in (C). n=10 for each group.* ***(D and E)*** *Image sequences taken from the ROIs in cells showing in (C).* ***(F)*** *Model of IST1 localization to endosomal microdomains when co-assembled with SNX15 or CHMP1B, and IST1 function in endosomal recycling. Scale bars in the whole cells and/or insets are as follows: (A-B) 25 µm and 1 µm, respectively; (C-E) 25 µm and 0.5 µm respectively.*

Figure 1

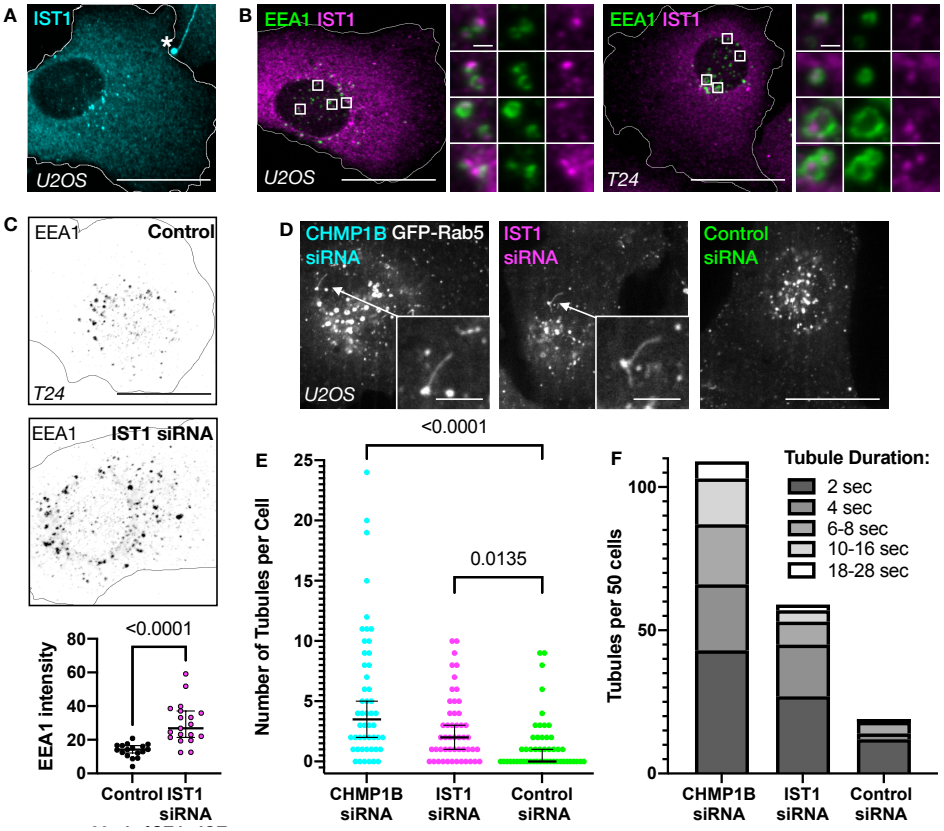
A
IST1
U2OS
B
EEA1 IST1
U2OS
EEA1 IST1
T24
C
EEA1
Control
T24
EEA1
IST1 siRNA
<0.0001
EEA1 intensity
80
60
40
20
0
Control
IST1 siRNA
D
CHMP1B GFP-Rab5
siRNA
U2OS
IST1
siRNA
Control
siRNA
E
<0.0001
0.0135
Number of Tubules per Cell
25
20
15
10
5
0
CHMP1B siRNA
IST1 siRNA
Control siRNA
F
Tubule Duration:
2 sec
4 sec
6-8 sec
10-16 sec
18-28 sec
Tubules per 50 cells
100
50
0
CHMP1B siRNA
IST1 siRNA
Control siRNA

Figure 2

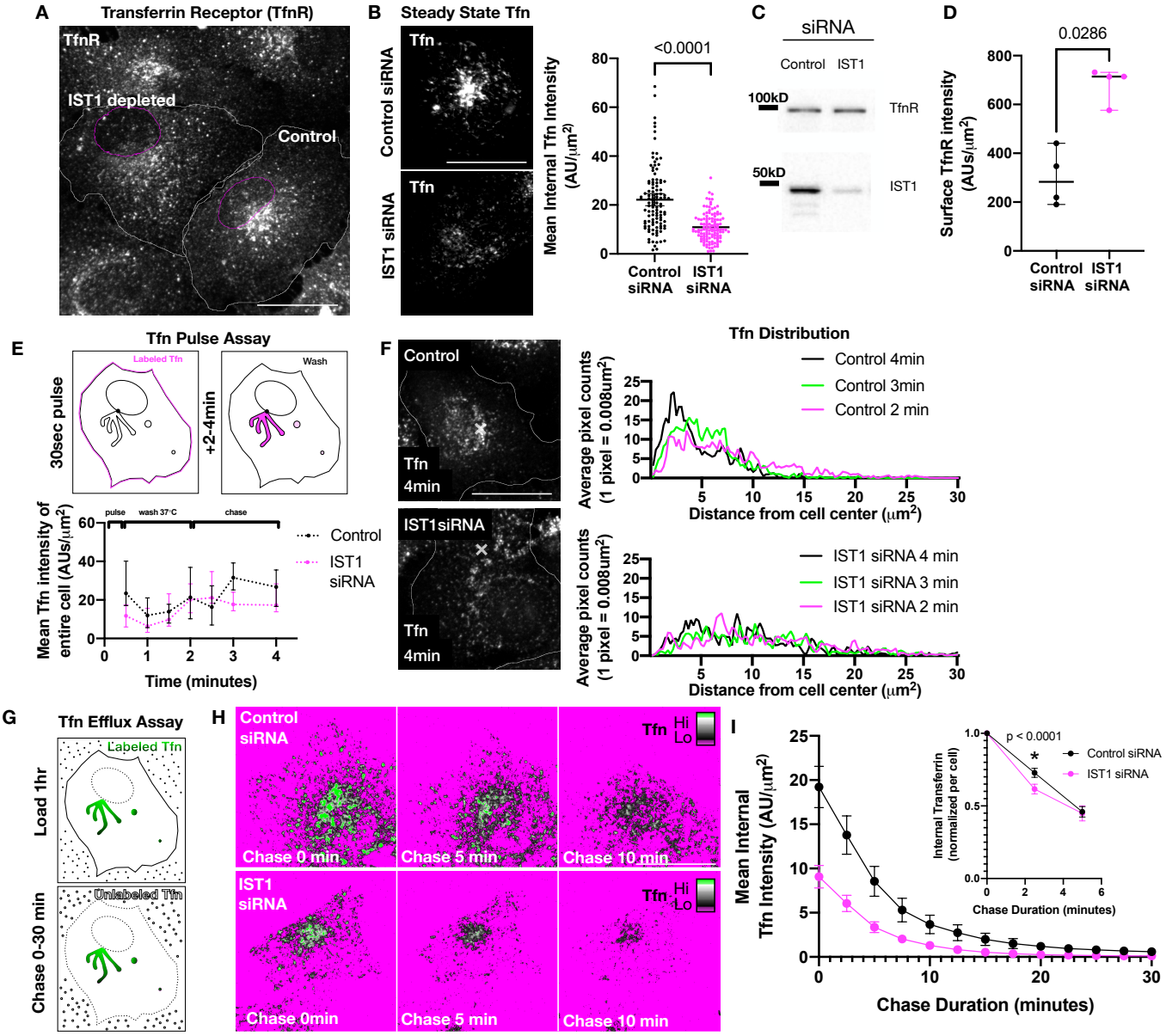
A
Transferrin Receptor (TfnR)
TfnR
IST1 depleted
Control
B
Steady State Tfn
Control siRNA
IST1 siRNA
Tfn
Mean Internal Tfn Intensity (AU/μm²)
<0.0001
Control siRNA
IST1 siRNA
C
siRNA
Control
IST1
100kD
50kD
TfnR
IST1
D
Surface TfnR intensity (AUs/μm²)
0.0286
Control siRNA
IST1 siRNA
E
Tfn Pulse Assay
30sec pulse
Labeled Tfn
+2-4min
Wash
Mean Tfn intensity of entire cell (AUs/μm²)
pulse
wash 37°C
chase
Control
IST1 siRNA
Time (minutes)
F
Control
Tfn 4min
IST1siRNA
Tfn 4min
Tfn Distribution
Control 4min
Control 3min
Control 2 min
IST1 siRNA 4 min
IST1 siRNA 3 min
IST1 siRNA 2 min
Average pixel counts (1 pixel = 0.008um²)
Distance from cell center (μm²)
G
Tfn Efflux Assay
Load 1hr
Chase 0-30 min
Labeled Tfn
Unlabeled Tfn
H
Control siRNA
IST1 siRNA
Tfn
Hi
Lo
Chase 0 min
Chase 5 min
Chase 10 min
Chase 0min
I
Mean Internal Tfn Intensity (AU/μm²)
Chase Duration (minutes)
p < 0.0001
Control siRNA
IST1 siRNA
Internal Transferrin (normalized per cell)

Figure 3

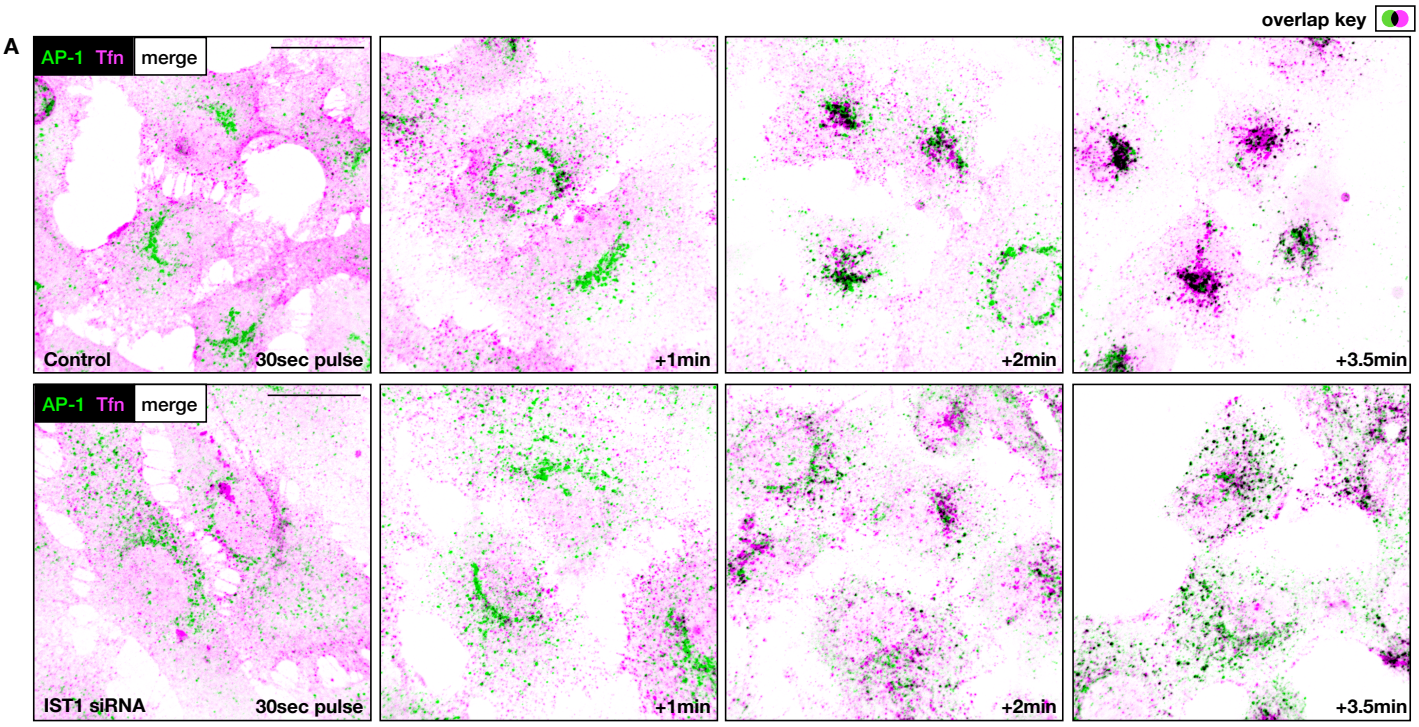
A
overlap key
AP-1 Tfn merge
Control
30sec pulse
+1min
+2min
+3.5min
IST1 siRNA
30sec pulse
+1min
+2min
+3.5min

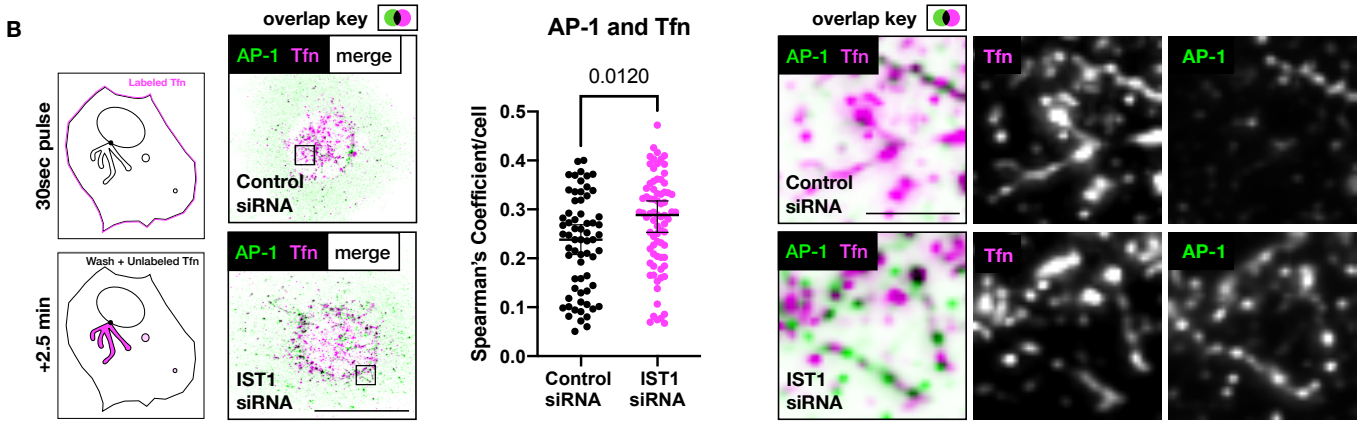
B
overlap key
30sec pulse
Labeled Tfn
+2.5 min
Wash + Unlabeled Tfn
AP-1 Tfn merge
Control siRNA
IST1 siRNA
AP-1 and Tfn
0.0120
Spearman's Coefficient/cell
0.5
0.4
0.3
0.2
0.1
0.0
Control siRNA
IST1 siRNA
Tfn
AP-1

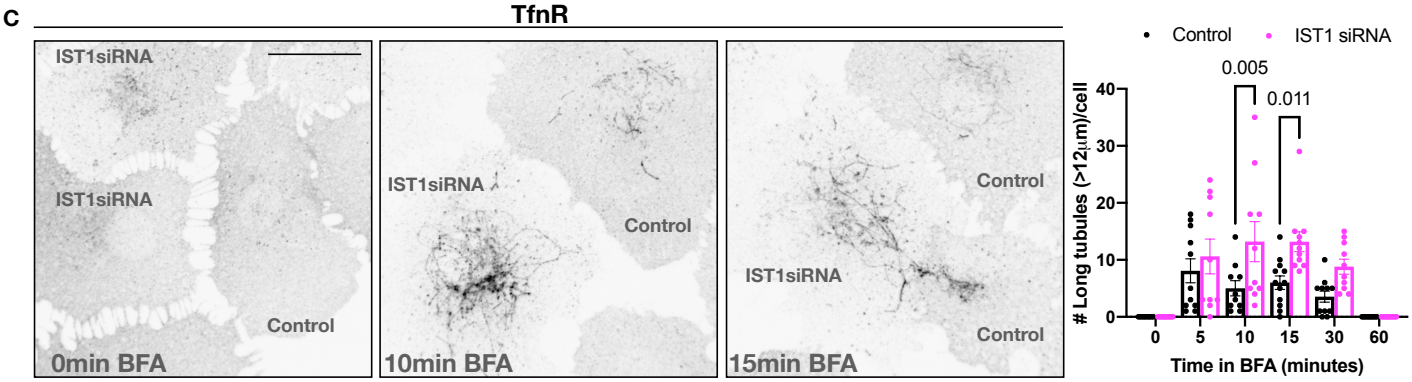
C
TfnR
IST1siRNA
Control
0min BFA
10min BFA
15min BFA
Control
IST1 siRNA
0.005
0.011
Long tubules (>12μm)/cell
40
30
20
10
0
0
5
10
15
30
60
Time in BFA (minutes)

Figure 4

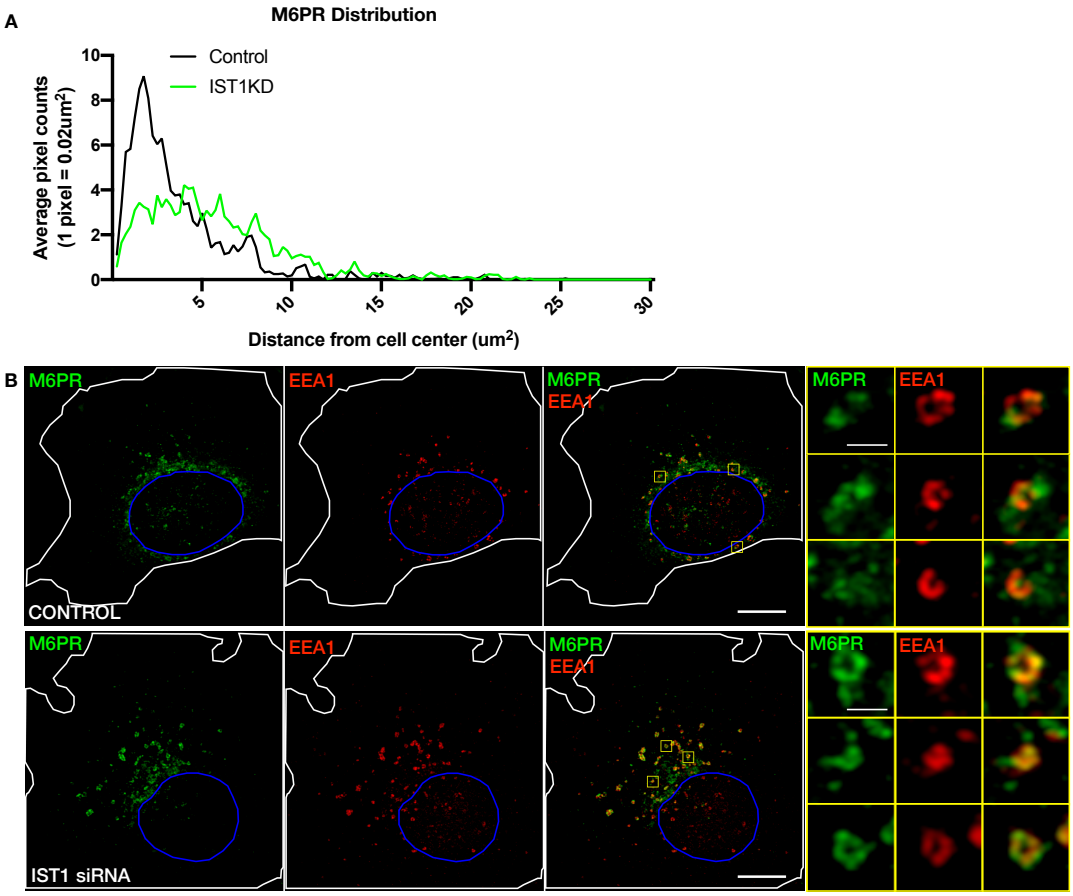
A
M6PR Distribution
Control
IST1KD
Average pixel counts
(1 pixel = 0.02um²)
0
2
4
6
8
10
5
10
15
20
25
30
Distance from cell center (um²)
B
M6PR
EEA1
M6PR
EEA1
CONTROL
IST1 siRNA

Figure 5

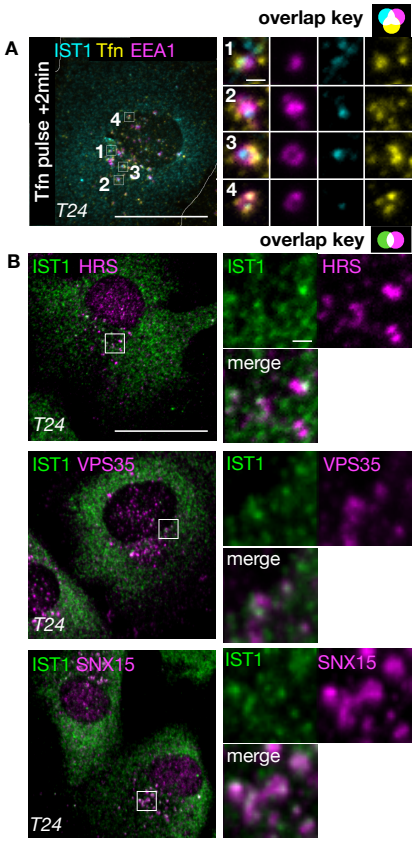
overlap key
A
IST1 Tfn EEA1
Tfn pulse +2min
T24
1
2
3
4
overlap key
B
IST1 HRS
IST1
HRS
merge
IST1 VPS35
IST1
VPS35
merge
IST1 SNX15
IST1
SNX15
merge

Figure 6

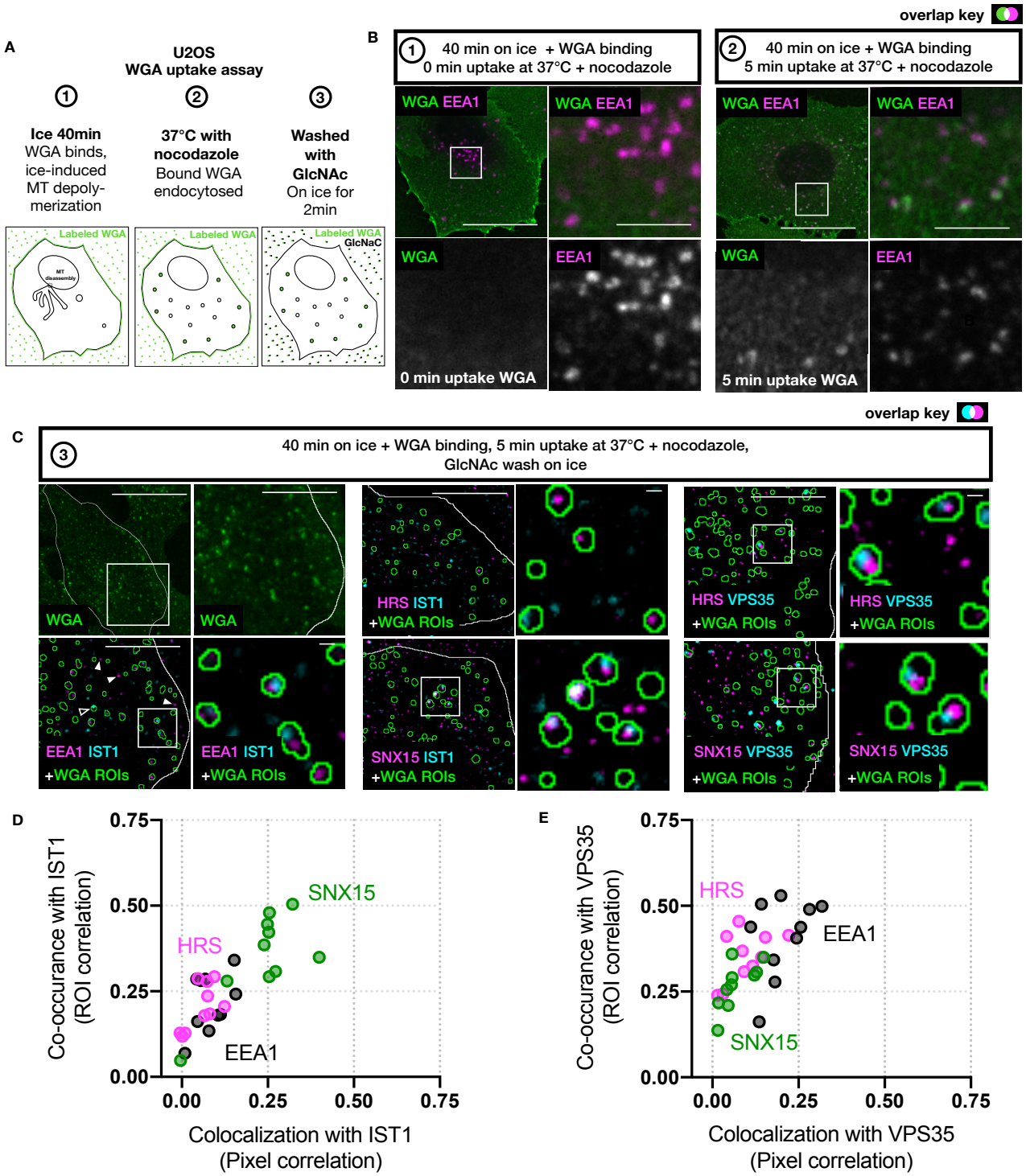
A
U2OS
WGA uptake assay
1
Ice 40min
WGA binds, ice-induced MT depoly-merization
2
37°C with nocodazole
Bound WGA endocytosed
3
Washed with GlcNAc
On ice for 2min
Labeled WGA
MT disassembly
Labeled WGA
Labeled WGA
GlcNAc
B
overlap key
1 40 min on ice + WGA binding
0 min uptake at 37°C + nocodazole
2 40 min on ice + WGA binding
5 min uptake at 37°C + nocodazole
WGA EEA1
WGA EEA1
WGA EEA1
WGA EEA1
WGA
EEA1
WGA
EEA1
0 min uptake WGA
5 min uptake WGA
C
overlap key
3 40 min on ice + WGA binding, 5 min uptake at 37°C + nocodazole,
GlcNAc wash on ice
WGA
WGA
HRS IST1
+WGA ROIs
HRS VPS35
+WGA ROIs
HRS VPS35
+WGA ROIs
EEA1 IST1
+WGA ROIs
EEA1 IST1
+WGA ROIs
SNX15 IST1
+WGA ROIs
SNX15 VPS35
+WGA ROIs
SNX15 VPS35
+WGA ROIs
D
Co-occurance with IST1
(ROI correlation)
0.75
0.50
0.25
0.00
SNX15
HRS
EEA1
0.00
0.25
0.50
0.75
Colocalization with IST1
(Pixel correlation)
E
Co-occurance with VPS35
(ROI correlation)
0.75
0.50
0.25
0.00
HRS
EEA1
SNX15
0.00
0.25
0.50
0.75
Colocalization with VPS35
(Pixel correlation)

Figure 7

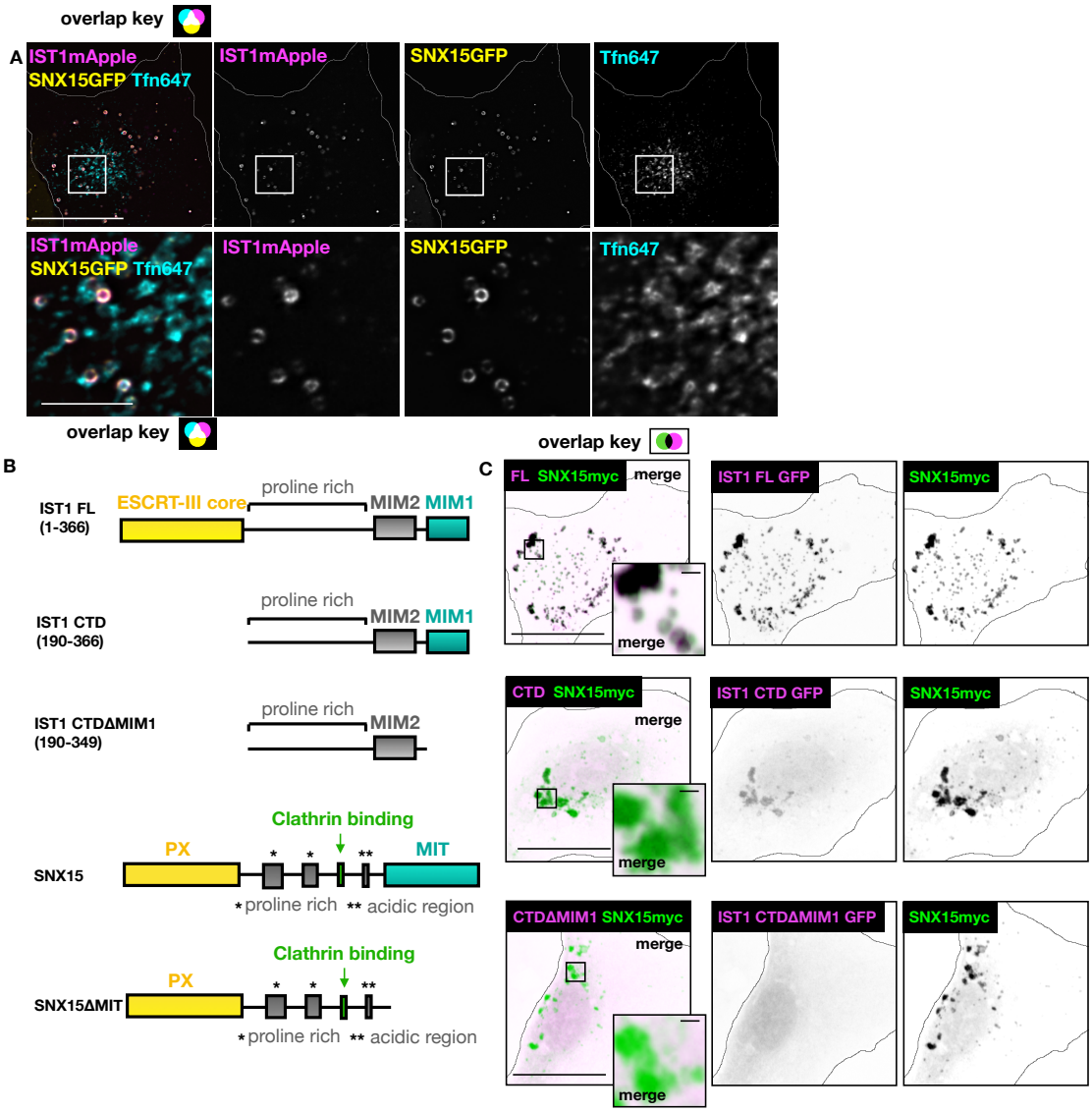
overlap key
A
IST1mApple
SNX15GFP Tfn647
IST1mApple
SNX15GFP
Tfn647
IST1mApple
SNX15GFP Tfn647
IST1mApple
SNX15GFP
Tfn647
overlap key
B
IST1 FL
(1-366)
ESCRT-III core
proline rich
MIM2 MIM1
IST1 CTD
(190-366)
proline rich
MIM2 MIM1
IST1 CTDΔMIM1
(190-349)
proline rich
MIM2
Clathrin binding
SNX15
PX
MIT
* proline rich ** acidic region
Clathrin binding
SNX15ΔMIT
PX
* proline rich ** acidic region
overlap key
C
FL SNX15myc
merge
merge
IST1 FL GFP
SNX15myc
CTD SNX15myc
merge
merge
IST1 CTD GFP
SNX15myc
CTDΔMIM1 SNX15myc
merge
merge
IST1 CTDΔMIM1 GFP
SNX15myc

Figure 8

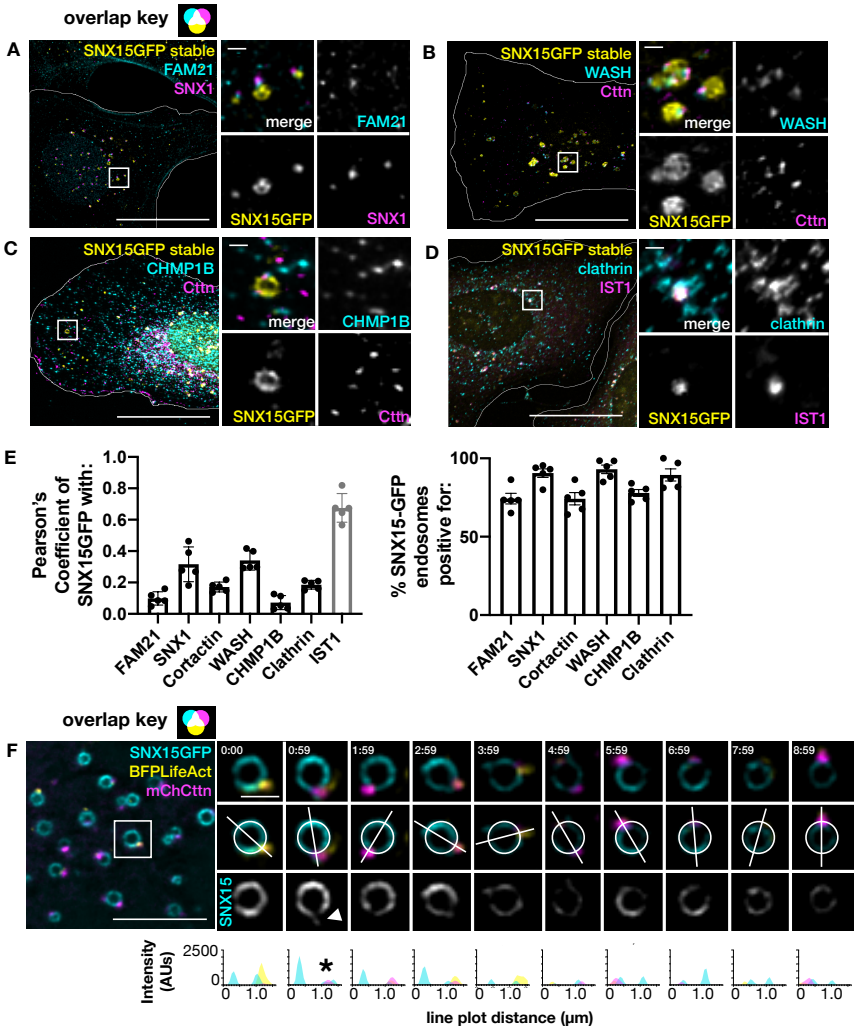
overlap key
A
SNX15GFP stable
FAM21
SNX1
merge
FAM21
SNX15GFP
SNX1
B
SNX15GFP stable
WASH
Cttn
merge
WASH
SNX15GFP
Cttn
C
SNX15GFP stable
CHMP1B
Cttn
merge
CHMP1B
SNX15GFP
Cttn
D
SNX15GFP stable
clathrin
IST1
merge
clathrin
SNX15GFP
IST1
E
Pearson's Coefficient of SNX15GFP with:
1.0
0.8
0.6
0.4
0.2
0.0
FAM21
SNX1
Cortactin
WASH
CHMP1B
Clathrin
IST1
% SNX15-GFP endosomes positive for:
100
50
0
FAM21
SNX1
Cortactin
WASH
CHMP1B
Clathrin

overlap key
F
SNX15GFP
BFPLifeAct
mChCttn
0:00
0:59
1:59
2:59
3:59
4:59
5:59
6:59
7:59
8:59
SNX15
Intensity (AUs)
2500
0
0
1.0
line plot distance (µm)

Figure 9

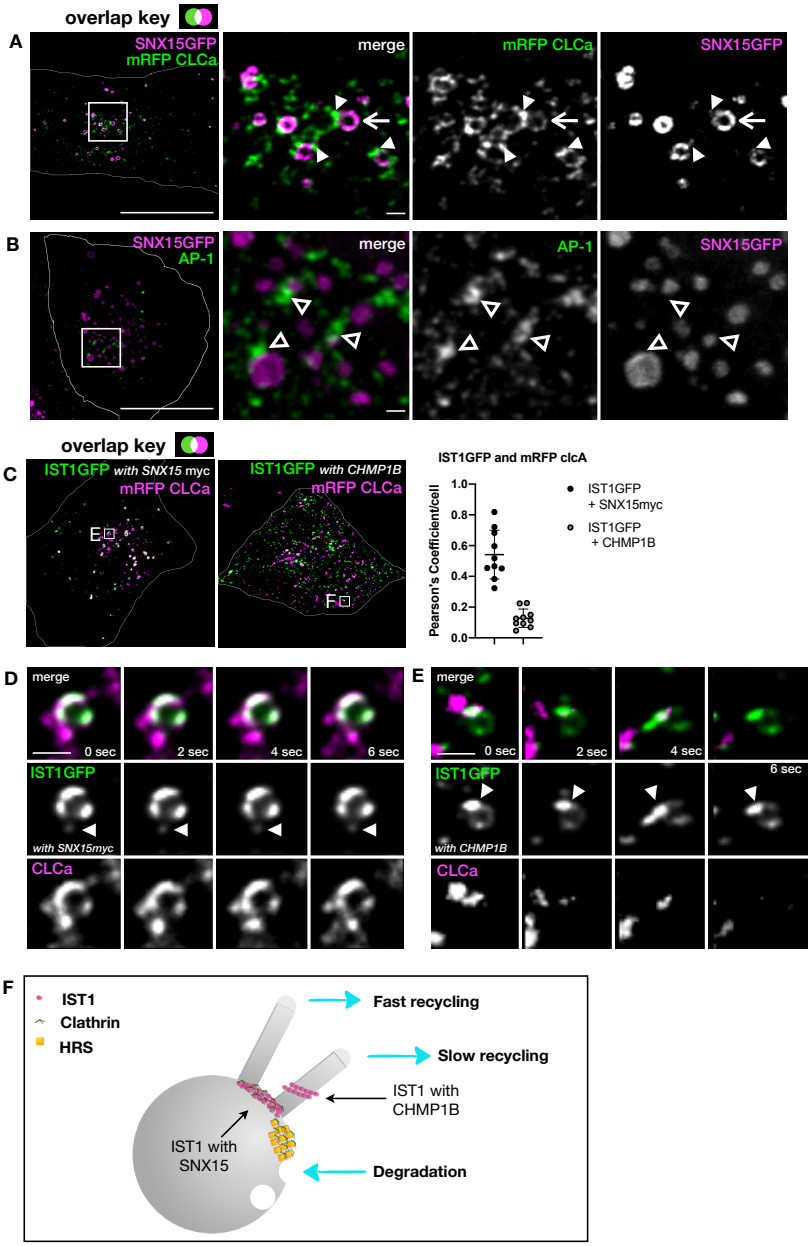
overlap key
A
SNX15GFP
mRFP CLCa
merge
mRFP CLCa
SNX15GFP
B
SNX15GFP
AP-1
merge
AP-1
SNX15GFP
overlap key
C
IST1GFP with SNX15 myc
mRFP CLCa
E
IST1GFP with CHMP1B
mRFP CLCa
F
IST1GFP and mRFP clcA
Pearson's Coefficient/cell
1.0
0.8
0.6
0.4
0.2
0.0
IST1GFP
+ SNX15myc
IST1GFP
+ CHMP1B
D
merge
0 sec
2 sec
4 sec
6 sec
IST1GFP
with SNX15myc
CLCa
E
merge
0 sec
2 sec
4 sec
6 sec
IST1GFP
with CHMP1B
CLCa

F
IST1
Clathrin
HRS
Fast recycling
Slow recycling
IST1 with
CHMP1B
IST1 with
SNX15
Degradation